Hindawi
International Journal of Photoenergy
Volume 2024, Article ID 5188636, 23 pages
https://doi.org/10.1155/2024/5188636

Research Article

Investigation of the Performance of a Sb_2S_3-Based Solar Cell with a Hybrid Electron Transport Layer (h-ETL): A Simulation Approach Using SCAPS-1D Software

Pierre Gérard Darel Kond Ngue,[1] **Ariel Teyou Ngoupo**,[1] **Aimé Magloire Ntouga Abena**,[1] **François Xavier Abomo Abega**,[2] **and Jean-Marie Bienvenu Ndjaka**[1]

[1]*University of Yaoundé I, Faculty of Science, Department of Physics, P.O. Box: 812, Yaoundé, Cameroon*
[2]*University of Ebolowa, Higher Institute of Agriculture, Forestry, Water and Environment (HIAFWE), P.O. Box: 118, Ebolowa, Cameroon*

Correspondence should be addressed to Ariel Teyou Ngoupo; arielteyou@yahoo.fr

Received 13 September 2023; Revised 28 February 2024; Accepted 19 March 2024; Published 8 April 2024

Academic Editor: Qiliang Wang

In order to reduce current leakage and improve electron transfer in solar cells, charge transport layers (CTL), mainly hybrid electron transport layers (*h*-ETL), are considered as a solution. In this research contribution, computational analysis using SCAPS-1D software is performed to explore the output photovoltaic parameters of a Sb_2S_3-based solar cell with *h*-ETL. No theoretical works on this configuration have been previously reported. The main objectives of the present work are to propose a *h*-ETL with good band alignment with the Sb_2S_3 absorber, high transparency, and Cd free; to mitigate the instability and cost issues associated with using Spiro-OMeTAD HTL; and to optimize the solar cell. Thus, we calibrated the *J-V* characteristics and electrical parameters of the FTO/(ZnO/TiO_2)/Sb_2S_3/Spiro-OMeTAD/Au solar cell by numerical simulation and compared them with those of the experiment. Subsequently, our simulations show that to replace the TiO_2 ETL used in the experiment and to form the *h*-ETL with ZnO, IGZO is found to be a good candidate. It has better band alignment with the Sb_2S_3 absorber than TiO_2 ETL, which reduces the trap states at the ETL/Sb_2S_3 interface; it has high transparency due to its wide bandgap; and an intense electric field is generated at the IGZO/Sb_2S_3 interface, which reduces the recombination phenomenon at this interface. MoO_3, $MASnBr_3$, Cu_2O, CuI, and CuSCN HTL were also tested to replace the Spiro-OMeTAD HTL. Simulation results show that the cell with MoO_3 HTL achieves higher performance due to its high hole mobility and high quantum efficiency in the visible region; it also allows the solar cell to have better thermal stability (TC = −0.32%/K) than the cell with Spiro-OMeTAD HTL (TC = −0.53%/K). The parameters that could improve the solar cell efficiency (η) obtained after these substitutions were also optimized. In particular, the parameters of the Sb_2S_3 absorber layer (thickness, defect density, and doping), ETL and HTL layer thicknesses, *h*-ETL/Sb_2S_3 interface defect density, and series and shunt resistances have been optimized. Finally, by combining high performance and thermal stability, the results show that the thermal stability of the solar cell depends on the back contact type; thus, nickel (Ni) was found to combine high performance and better thermal stability among the back contacts investigated. After these improvements, the efficiency of the Sb_2S_3-based solar cell increased from 5.08% (J_{SC} = 16.19 mA/cm^2, V_{OC} = 0.56 V, and FF = 55.40%) to 15.43% (J_{SC} = 18.51 mA/cm^2, V_{OC} = 1.11 V, and FF = 74.76%). This study proposes an approach to optimize the Sb_2S_3 upper subcell for tandem solar cells.

1. Introduction

Interest in solar cells based on antimony trisulfide (Sb_2S_3) is growing due to the exceptional optoelectronic properties of this new emerging photovoltaic material. Sb_2S_3 is a p-type semiconductor with a high absorption coefficient ($\alpha > 10^5$ cm^{-1}) in visible light [1] and an appropriate bandgap (1.7-1.8 eV) for the upper subcell in double-junction tandem solar cells [2]. Furthermore, Sb_2S_3 is a binary compound without secondary phases, and due to its low melting point (~550°C), layers of high crystalline quality can be synthesized at low temperatures (<350°C) [2]. In

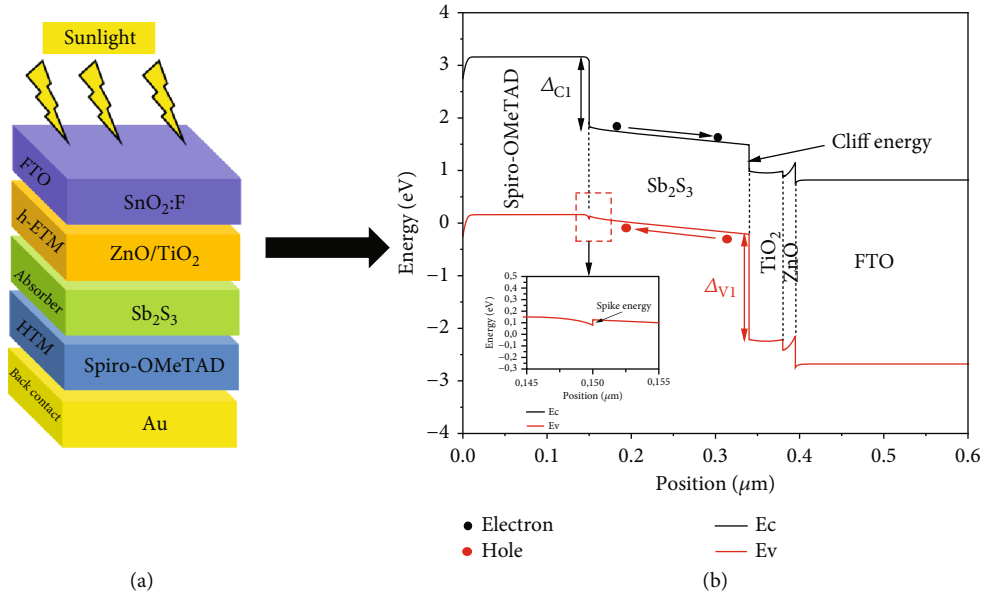

Figure 1: (a) Modeled structure of a solar cell based on Sb_2S_3 [23] and (b) energy band diagram.

addition to these properties, Sb_2S_3 has the advantage of being composed of nontoxic elements that are abundant on Earth, making it an ideal absorber for the design of more environmentally friendly heterojunction solar cells. In contrast to nanostructured films, Sb_2S_3 thin films can be synthesized by various deposition methods such as chemical bath deposition [3], sputtering and thermal evaporation [4], spin coating [5], atomic layer deposition [6], close-space sublimation [7], and radio frequency spraying [8].

The application of antimony trisulfide (Sb_2S_3) as an absorber in planar solar cells was realized for the first time in 1993 by Kondrotas et al. [2]. They obtained a conversion efficiency of 5.19% for the Au-Al/p-Si(111)/Sb_2S_3/grid-Cu-graphite configuration by synthesizing Sb_2S_3 by chemical bath deposition (CBD) on a p-type oriented (111) silicon substrate and annealing it at 350°C. In 1994, Kondrotas et al. also explored the possibility of fabricating Schottky-type devices. They found that the Schottky barrier height is virtually independent of the metal work function, despite similar annealing conditions. For the ITO/Sb_2S_3/Pt configuration, an efficiency of 5.5% was obtained [2]. Their findings show that by modifying the structure and manufacturing conditions, the performance of the devices can be improved, opening up new perspectives for the use of Sb_2S_3 in the field of solar energy. However, it was only in 2009 that researchers turned their attention back to the Sb_2S_3 absorber. In 2014, Kim et al. reported a conversion efficiency of 5.77% for a FTO/c-TiO_2/Sb_2S_3/P3HT/PEDOT:PSS/Au planar heterojunction solar cell using atomic layer deposition (ALD) and heat treatment at 330°C [9]. The results show that controlling the thickness, density, and purity of the absorber can reduce the reverse recombination phenomena by significantly suppressing the oxide defects in Sb_2S_3 sensitizers, which greatly improves the conversion efficiency. In 2018, Jiang et al. [10] showed that doping the Sb_2S_3 layer with Cs^+ ions significantly improves the conversion efficiency, carrier concentration, crystallinity, and quality of the Sb_2S_3 film by reducing carrier recombination. Their FTO/TiO_2/Sb_2S_3/Spiro-OMeTAD/Au solar cell efficiency was 6.56%. More recently, in 2020, Han et al. [11] proposed the surface passivation of Sb_2S_3 films with an inorganic $SbCl_3$ gel to reduce the surface defects and nonradiative recombination and thus achieved a record conversion efficiency of 7.1%. To date, no other Sb_2S_3-based planar heterojunction structure has been able to exceed this conversion efficiency, which is well below the theoretical value of 28.64% predicted by the Shockley-Queisser limit for solar cells with a 1.7 eV bandgap absorber [2].

Studies have shown that interdiffusion between layers, nonideal series and shunt resistances, interfaces and nonradiative recombination phenomena, deep defects, etc., are the main obstacles to achieve high efficiency in Sb_2S_3-based solar cells [12]. Therefore, to improve the performance of Sb_2S_3-based solar cells, major challenges regarding the properties of various materials and structures need to be overcome. In order to reduce these limitations and to understand how the different parameters of interest for the solar cell affect its performance, numerical simulation seems to be a necessary tool. This is the purpose of many modeling and simulation studies [12–17] that have been carried out in recent years. The results show that controlling recombination phenomena (radiative and nonradiative) at the interfaces and in the absorber, parasitic absorptions, resistances (series and shunt), etc., are required to achieve high conversion efficiency. A common solution to reduce the leakage current is to use a double buffer layer. In fact, studies on perovskite-based solar cells show that the use of a bilayer electron transport layer (ETL), also called hybrid ETL [18–20], allows to reduce parasitic losses, improve charge injection, and reduce photocarrier recombination phenomena, thus improving the conversion efficiency [18–22]. Based on such considerations, Baron Jaimes et al. have proposed a functional ZnO/TiO_2 bilayer as a hybrid

Table 1: SCAPS-1D input parameters of the materials used in the simulation.

Parameters	FTO	ZnO	TiO_2	Sb_2S_3	Spiro-OMeTAD
Thickness w (μm)	0.27	0.015 [23]	0.04 [23]	0.190 [23]	0.150 [23]
Bandgap E_g (eV)	3.5 [27]	3.3 [23]	3.2 [23]	1.7 [23]	3 [23]
Electronic affinity χ_e (eV)	4.7 [23]	4.3 [23]	4.2 [23]	3.7 [23]	2.45 [23]
Dielectric constant ε_r	9 [44]	9 [44]	9 [43]	19	3 [48]
Conduction band state density N_C (cm^{-3})	2.2×10^{18} [44]	2.2×10^{18} [44]	10^{19} [27]	10^{19} [40]	10^{19} [48]
Valence band state density N_V (cm^{-3})	1.8×10^{19} [44]	1.8×10^{19} [44]	10^{19} [27]	10^{19} [40]	10^{19} [48]
Electron thermal velocity ν_{th_e} (cm/s)	1.1×10^{7} [49]	10^{7} [44]	10^{7} [27]	10^{7} [14]	10^{7} [27]
Hole thermal velocity ν_{th_h} (cm/s)	1.1×10^{7} [49]	10^{7} [44]	10^{7} [27]	10^{7} [14]	10^{7} [27]
Electron mobility μ_e (cm^2/Vs)	33 [44]	50 [44]	20 [43]	n [47]	10^{-4} [50]
Hole mobility μ_h (cm^2/Vs)	8 [44]	25 [44]	1 [2]	10 [47]	10^{-4} [50]
Donor density N_D (cm^{-3})	10^{18} [44]	10^{18} [44]	10^{17} [2]	—	—
Acceptor density N_A (cm^{-3})	—	—	—	2×10^{13} [47]	2×10^{18} [46]
Defect properties					
Defect type	Neutral	Neutral	Neutral	Neutral	Neutral
Capture cross-section of electrons/holes (cm^2)	10^{-19}	10^{-19}	10^{-19}	1.950×10^{-14}	10^{-15}
Energy distribution	Single	Single	Single	Single	Single
Reference for defective energy level E_t	Above Ev	Above Ev	Above Ev	Above Ev	Above Ev
Energy level with respect to a reference (eV)	0.6	0.6	0.6	0.85	0.6
Total defect N_t ($1/cm^3$)	10^{17} [44]	10^{17} [44]	10^{15} [43]	1.1×10^{16}	10^{15} [50]
TiO_2/Sb_2S_3 interface properties					
Defect type			Neutral		
Capture cross-section of electrons/holes (cm^2)			1.00×10^{-13}		
Energy distribution			Single		
Reference for defective energy level E_t			Midgap		
Energy level with respect to a reference (eV)			0.6		
Total defect N_t ($1/cm^2$)			2.00×10^{15}		
Contact properties	Front contact			Rear contact	
Electron surface recombination velocity (cm/s)	10^{5}			10^{5}	
Hole surface recombination velocity (cm/s)	10^{7}			10^{7}	
Metal work function (eV)	4.7			5.2 [45]	
Majority carrier barrier height relative to E_F (eV)	-0.03			0.25	
Majority carrier barrier height relative to E_V or E_C	-0.0504			0.2083	

ETL in a Sb_2S_3-based planar solar cell [23]. It was found that this structure has a higher efficiency (5.08%) than that based on a monolayer of ZnO ETL and TiO_2 ETL, which have efficiencies of 0.15% and 3.84%, respectively [23]. Among several numerical simulation studies on Sb_2S_3 solar cell for its performance optimization [12–17], to the best of our knowledge, none of these studies have analyzed this cell with a hybrid ETL.

Based on the experimental work of Baron Jaimes et al. [23], this study focuses on the modeling and numerical analysis of a Sb_2S_3-based solar cell with a ZnO/TiO_2 hybrid buffer layer (or hybrid electron transport layer, h-ETL) and Spiro-OMeTAD as hole transport layer (HTL). However, TiO_2 ETL has low conductivity and mobility [23, 24] and poor band alignment with the Sb_2S_3 absorber. In addition, TiO_2 is susceptible to photocatalysis when exposed to UV light; this reduces the long-term stability of the material [24]. Spiro-OMeTAD HTL, on the other hand, presents problems of instability and cost. This limits the performance of this solar cell and makes it difficult to mass-produce. Therefore, the main objective of this work is firstly to propose the best ETL and HTL materials that can substitute TiO_2 and Spiro-OMeTAD, respectively, and that will optimize such a solar cell structure. In addition, special attention is paid to the long-term stability of the back contact. Another interesting aspect of this study is that we want to combine the high performance of the Sb_2S_3 solar cell with the best possible thermal stability. This is a new approach to solar cell performance improvement. This approach is different from other studies where back contact is optimized only from an efficiency point of view [14, 15, 25–29]. Furthermore, the optimization of other parameters of interest such as the thickness, doping, bulk defects of the Sb_2S_3 absorber, the density of states

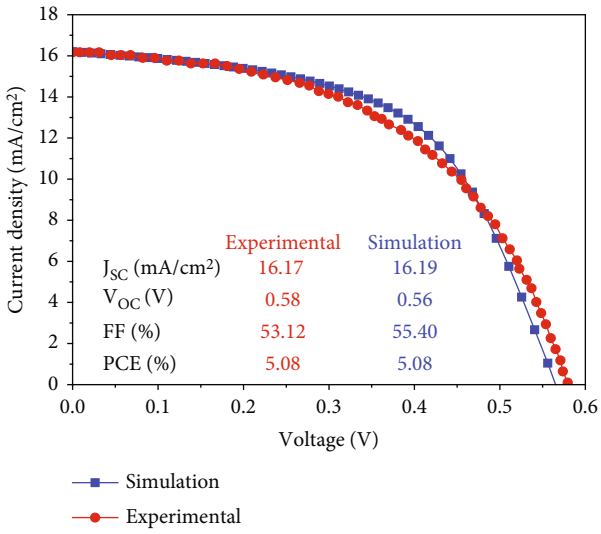

Figure 2: Experimental and simulated J-V curves of a Sb_2S_3-based solar cell.

Table 2: Experimental and simulated performance parameters of a Sb_2S_3-based solar cell.

Parameters	Experimental [23]	Simulation
J_{SC} (mA/cm^2)	16.17	16.19
V_{OC} (V)	0.58	0.56
FF (%)	53.12	55.40
η (%)	5.08	5.08

of the ETL/Sb_2S_3 interface, and the series and shunt resistances will also be addressed in this work.

2. Structure of the Device and Simulation Method

Photovoltaic researchers use several software programs to analyze the performance of thin-film solar cells. These include AMPS [30], SILVACO ATLAS [31], COMSOL [32], wxAMPS [33], PC1D [34], and SCAPS-1D [35]. In this work, we chose to use the one-dimensional simulation software SCAPS-1D (version 3.3.10) developed at the University of Gent in Belgium by Burgelman et al. [36]. This software has several advantages, including the ability to analyze the structure of up to seven different layers and perform deep and batch analysis and an easy-to-use interface. Furthermore, the results obtained from this software are in agreement with the experimental data reported by other research groups [37–41], making it a reliable tool for analyzing solar cell performance. The SCAPS-1D software is based on the numerical solution of fundamental semiconductor equations, including the Poisson equation (Equation (1)), the continuity equations of electrons (Equation (2)), and holes (Equation (3)) [39]: these are three coupled and nonlinear differential equations, so the solutions allow to obtain the electrical parameters of the solar cell.

$$\frac{\partial}{\partial x}\left(\varepsilon_0\varepsilon\frac{\partial\psi}{\partial x}\right) = -q\left(p - n + N_D^+ - N_A^- + \frac{\rho_{\_def}}{q}\right), \quad (1)$$

$$-\frac{\partial J_n}{\partial x} - U_n + G = \frac{\partial n}{\partial t}, \quad (2)$$

$$-\frac{\partial J_p}{\partial x} - U_p + G = \frac{\partial p}{\partial t}. \quad (3)$$

Equation (1) describes the phenomena of electrostatic nature, where ψ is the electrostatic potential; n and p are the densities of free electrons and holes, respectively; and N_D^+ and N_A^- are the concentrations of ionized donor and acceptor, respectively. Equations (2) and (3) govern the dynamic equilibrium condition in a semiconductor, where G is the generation rate; U_n and U_p are the recombination rates of electrons and holes, respectively; and J_n and J_p are the current densities of electrons and holes, respectively; their terms are found in literature [42].

The Sb_2S_3-based solar cell modeled in this study is the FTO/(ZnO/TiO_2)/Sb_2S_3/Spiro-OMeTAD/Au structure from the experimental work of Baron Jaimes et al. [23], as shown in Figure 1(a); it corresponds to a stack of layers of semiconductor materials. Fluorine-doped tin oxide (FTO) is used as the transparent conductive oxide; ZnO/TiO_2 forms the hybrid electron transport layer (h-ETL), also known as the hybrid buffer layer, which combines two electron transport layers (ETL) acting as the hole blocking layer; Spiro-OMeTAD is the electron-blocking layer or hole transport layer (HTL), and gold (Au) is the rear contact. The p-type Sb_2S_3 absorber layer, which is responsible for the photovoltaic conversion, is located between the h-ETL and HTL materials. Series and shunt resistances are fixed at 2.7 $\Omega\cdot$cm^2 and 4.35×10^2 $\Omega\cdot$cm^2 [23]. Table 1 lists the input parameters required to model our device, these values have been taken within literature [2, 14, 23, 27, 40, 43–50], and some are the reasonable estimation. All simulations were carried out under the AM1.5 irradiation spectrum, the operational temperature taken at 300 K (except for the effect of operating temperature), and in the absence of polarization.

Figure 1(b) shows the energy band diagram of the solar cell; this diagram provides information about the dynamics of the charge carriers in the solar cell. By the mechanisms of diffusion (due to the integrated potential) and drift (due to the presence of electric fields at the interfaces), electrons are attracted to the ETL layer and holes are attracted to the HTL layer. They are collected by the front and back contacts, respectively. The conduction band (ΔC_1) and valence band (ΔV_2) offsets act as blocking barriers for minority carriers (Figure 1(b)). These band offsets at the TiO_2/Sb_2S_3 and Sb_2S_3/Spiro-OMeTAD interfaces indicate the presence of a cliff and a spike, respectively. These mismatches of energy bands significantly affect the performance parameters, including J_{SC}, V_{OC}, FF, and PCE [51].

3. Results and Discussion

3.1. Comparison of J-V Characteristics between Simulation and Experiment. In order to validate our simulation

Table 3: Input parameters of the different ETL materials.

Parameter	CdS [48]	$Cd_{0.5}Zn_{0.5}S$ [48]	IGZO [48]	PCBM [48]
Thickness w (μm)	0.04	0.04	0.04	0.04
Bandgap E_g (eV)	2.4	2.8	3.05	2
Electronic affinity χ_e (eV)	4.2	3.8	4.16	3.9
Dielectric constant ε_r	10.0	10.0	10.0	3.9
Conduction band state density N_C (cm^{-3})	2.2×10^{18}	10^{18}	5×10^{18}	2.5×10^{21}
Valence band state density N_V (cm^{-3})	1.8×10^{19}	10^{18}	5×10^{18}	2.5×10^{21}
Electron thermal velocity ν_{th_e} (cm/s)	10^7	10^7	10^7	10^7
Hole thermal velocity ν_{th_h} (cm/s)	10^7	10^7	10^7	10^7
Electron mobility μ_e (cm^2/Vs)	100	100	15	0.2
Hole mobility μ_h (cm^2/Vs)	25	25	0.1	0.2
Donor density N_D (cm^{-3})	10^{17}	10^{17}	10^{18}	2.93×10^{17}
Total defect N_t (cm^{-3})	10^{17}	10^{15}	10^{15}	10^{15}

parameters (Table 1), we compared our simulation results obtained via the SCAPS-1D software with those experimental proposed by Baron Jaimes et al. [23]. Thus, we first compared the J-V curve of the experimental work to that resulting from the simulation, as illustrated in Figure 2: the J-V curves show a similar trend. Then, the solar cell electrical parameters (open-circuit voltage (V_{OC}), short-circuit current density (J_{SC}), fill factor (FF), and efficiency (η)) were compared with the experimental results (Table 2). Thus, there is a concordance between the experimental values and the simulation results. The preceding elements thus confirm the validity of our solar cell model and the parameters listed in Table 1.

3.2. Effect of Different Electron Transport Layer (ETL) Materials on Solar Cell Performance. An electron transport layer (ETL) is a critical element in solar cells. It plays an important role in the extraction and transport of electrons, while also acting as a hole blocking layer that reduces carrier recombination [52]. It is therefore necessary to find a material which can best perform this function for high-efficiency solar cells. As previously reported, the TiO_2 ETL used in the solar cell (Figure 1(a)) has poor conductivity and mobility [23, 24] and poor band alignment with the Sb_2S_3 absorber; and its long-term stability is reduced under UV light exposure [24]. In this section, the effect of CdS, $Cd_{0.5}Zn_{0.5}S$, IGZO, and PCBM ETL materials as potential candidates for TiO_2 ETL replacement is investigated. The parameters of these ETL materials, which can form a hybrid electron transport layer with ZnO ETL, are listed in Table 3. Figures 3(a) and 3(b) show the J-V and quantum efficiency curves, respectively, associated with different ETL materials. Table 4 summarizes the electrical parameters for different ETL materials and shows that the solar cell achieves low efficiency when TiO_2 is replaced with CdS ETL (4.96%), and the maximum efficiency of 6.99% is achieved with IGZO ETL. The performance of the solar cell with PCBM ETL (organic material) is also remarkable, and the efficiency is 6.32%. CdS ETL and IGZO ETL quantum efficiency curves (Figure 3(b)) are nearly identical in the visible, with maximum quantum efficiencies of 80.67% and 81.06%, respectively. The high J_{SC} is due to the high electronic mobility of CdS, which favors carrier movement and collection.

The conduction band offset (CBO or ΔE_C), defined as the difference between the electronic affinities of two adjacent layers and given by Equation (4), is an important parameter for obtaining high-efficiency solar cells as mentioned in Section 2. The energy band diagrams show that for all investigated ETL materials (CdS, $Cd_{0.5}Zn_{0.5}S$, IGZO, and PCBM), energy cliff ($\Delta E_C < 0$) is formed at the ETL/Sb_2S_3 interface (Figure S1, Supporting Information). This energy cliff does not inhibit the flow of photogenerated electrons. However, the activation energy (E_a), which is the difference between the absorber bandgap and the absolute ΔE_C (Equation (5)), for carrier recombination becomes lower than the Sb_2S_3 absorber bandgap as the energy cliff increases. This leads to a predominance of recombination phenomena at the ETL/absorber interface in the solar cell [48]. It is also reported that E_a reduces V_{OC} [48]. The E_a value associated with each ETL is reported in Table 4. The results show that the CdS ETL provides the lowest activation energy (1.2 eV) and the solar cell has the lowest V_{OC}, which could justify the low solar cell efficiency. This was found to agree with Minemoto and Murata [53]. On the other hand, the IGZO ETL ($E_a = 1.24\,eV$) allows to obtain the highest conversion efficiency. This result could be due to its large bandgap (3.05 eV), which allows it to ensure high transparency to light and increase its absorption by the Sb_2S_3 active layer for better carrier generation (Figure S2.a), while allowing efficient electron extraction from this active layer [54]. Furthermore, the intense electric field at the IGZO/Sb_2S_3 interface (Figure S3), which separates more electron-hole pairs, coupled with the high donor concentration of IGZO ETL, which improves its conductivity, could sufficiently reduce the recombination phenomena at this interface (Figure S2.b) and improve the solar cell performance. According to Figure S1 and Table 4, a larger valence band

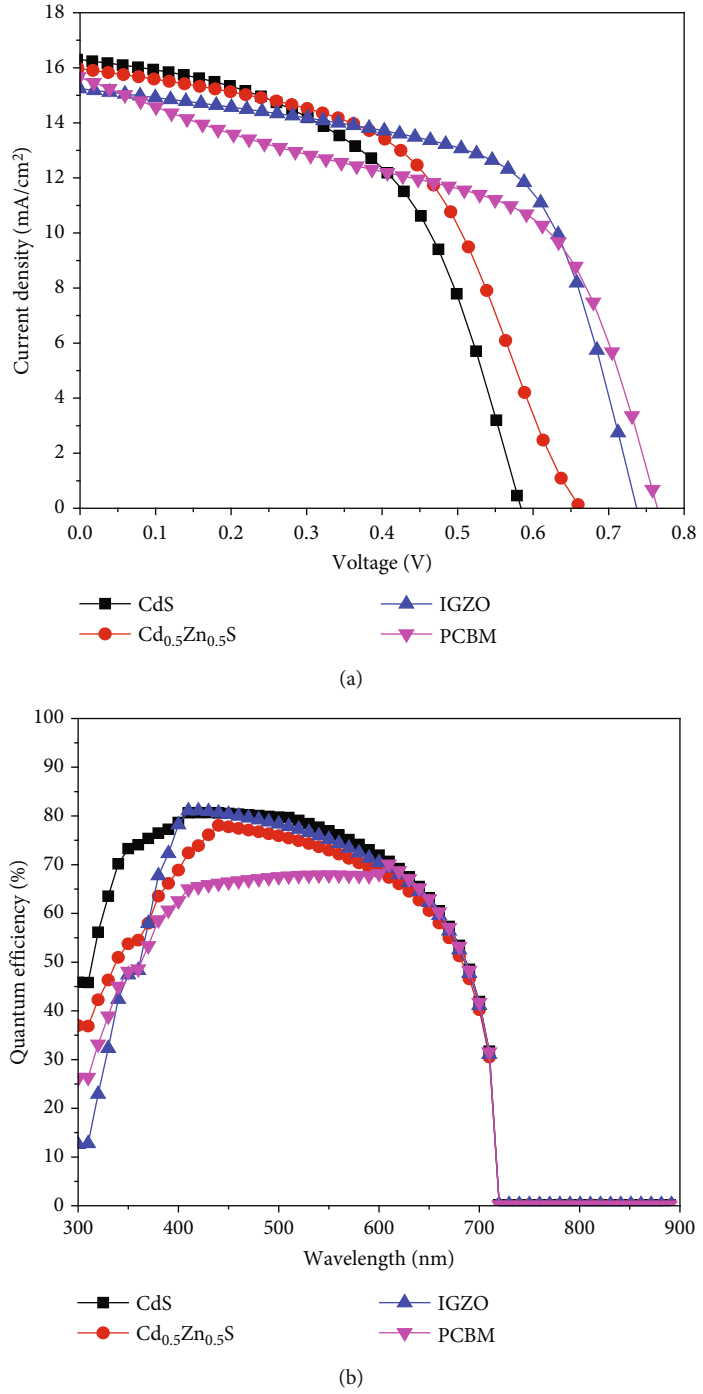

Figure 3: Effect of different ETL materials on (a) J-V characteristics and (b) quantum efficiency of a Sb_2S_3-based solar cell.

offset is observed at the ETL/absorber interface with IGZO ETL. This band offset acts as a potential barrier that prevents holes from recombining with electrons in the ETL material. This improves the efficiency of the solar cell. The $Cd_{0.5}Zn_{0.5}S$ ETL shows a better band alignment with the Sb_2S_3 absorber (Figure S1.b) compared to the other ETL materials (Figures S1.a, S1.c, and S1.d). It also has a high electron mobility (100 cm^2/Vs), and its activation energy (1.6 eV) is very close to the bandgap value of the Sb_2S_3 absorber (1.7 eV). Despite these properties, low electric field (Figure S3) and high recombination phenomena (Figure S2.b) hinder the solar cell conversion efficiency.

Therefore, the effect of different ETL materials shows that the solar cell achieves better performance when the TiO_2 ETL is replaced by an ETL with wide bandgap, low activation energy, intense electric field, and larger valence band offset at the ETL/Sb_2S_3 interface. The characteristics observed for the different ETL materials investigated (CdS, $Cd_{0.5}Zn_{0.5}S$, IGZO, and PCBM) are also attributed to the hybrid ETL (ZnO/ETL) present in the Sb_2S_3-based solar cell structure (Figure 1(a)).

Table 4: Simulated performance parameters and activation energy of a Sb_2S_3-based solar cell using different ETL materials.

	Electrical parameters						
ETL	J_{SC} (mA/cm^2)	V_{OC} (V)	FF (%)	η (%)	ΔE_c (eV)	ΔE_v (eV)	E_a (eV)
CdS	16.28	0.58	52.21	4.96	-0.5	1.2	1.2
$Cd_{0.5}Zn_{0.5}S$	15.96	0.66	52.53	5.56	-0.1	1.2	1.6
PCBM	15.64	0.76	52.78	6.32	-0.2	0.5	1.5
IGZO	15.23	0.73	62.18	6.99	-0.46	1.81	1.24

Table 5: SCAPS input parameters for HTL materials.

Parameter	CuSCN [37]	MoO_3 [37]	Cu_2O [27]	CuI [27]	$MASnBr_3$ [48]
Thickness w (μm)	0.15	0.15	0.15	0.15	0.15
Bandgap E_g (eV)	3.6	3	2.17	3.1	2.15
Electronic affinity χ_e (eV)	1.7	2.5	3.2	2.1	3.39
Dielectric constant ε_r	10.0	12.5	7.11	6.5	8.2
Conduction band state density N_C (cm^{-3})	2.2×10^{19}	2.2×10^{17}	2.02×10^{17}	2.8×10^{19}	10^{18}
Valence band state density N_V (cm^{-3})	1.8×10^{18}	2.2×10^{16}	1.1×10^{19}	1.0×10^{19}	10^{18}
Electron thermal velocity ν_{th_e} (cm/s)	10^7	10^7	10^7	10^7	10^7
Hole thermal velocity ν_{th_h} (cm/s)	10^7	10^7	10^7	10^7	10^7
Electron mobility μ_e (cm^2/Vs)	100	25	200	100	1.6
Hole mobility μ_h (cm^2/Vs)	25	100	80	43.9	1.6
Donor density N_D (cm^{-3})	0	0	0	0	0
Acceptor density N_A (cm^{-3})	10^{18}	10^{18}	10^{18}	10^{18}	10^{18}
Total defect N_t (1/cm^3)	10^{14}	10^{14}	10^{14}	10^{14}	10^{15}

$$\Delta E_C = \chi_{\_Sb_2S_3} - \chi_{\_ETL}, \tag{4}$$

$$E_a = E_{g\_Sb_2S_3} - |\Delta E_c|. \tag{5}$$

3.3. Effect of Different HTL Materials on Solar Cell Performance. Organic Spiro-OMeTAD HTL is widely used as hole transport layer (HTL) in solar cell design and fabrication but is subject to instability problems that degrade solar cell performance over time [27]. Therefore, finding a better HTL material to mitigate these problems is necessary. In Subsection 3.2, the effect of ETL material on solar cell performance was investigated using Spiro-OMeTAD HTL. In order to consider the combined effect of the previous ETL materials and the following HTL materials, MoO_3, $MASnBr_3$, Cu_2O, CuI, and CuSCN, whose parameters are given in Table 5, a total of twenty (20) configurations are simulated. The electrical parameters J_{SC}, V_{OC}, FF, and η are given in Tables S1, S2, S3, and S4 (Supporting Information), respectively. This ETL and HTL material selection method for solar cell optimization is widely reported [55–58]. Figure 4 presents the effect of all possible combinations between these ETL and HTL materials in order to determine the ETL-HTL pair that gives the best conversion efficiency of the solar cell. Consistent with Table S4, Figure 4 reveals that IGZO is the best ETL material, which is in agreement with the results in Subsection 3.2. For all different HTL materials, solar cell structures with IGZO ETL have better efficiency than other ETL materials. Thus, among the simulated configurations, a maximum efficiency of 7.44% (J_{SC} = 15.33 mA/cm^2; V_{OC} = 0.74 V; FF = 65.31%) is achieved with the IGZO ETL-MoO_3 HTL pair, while the minimum solar cell efficiency with IGZO ETL-CuI HTL is 7.03%. This difference in performance is due to the higher hole mobility of MoO_3 HTL (100 cm^2/Vs) compared to the other HTL materials tested.

Figure 5 depicts the effect of different HTL materials on the *J-V* characteristics and quantum efficiency curves of the Sb_2S_3 solar cell with ZnO/IGZO *h*-ETL. These curves display a similar trend, and Table 6 provides device electrical parameters. The determination of the valence band offset (VBO or ΔE_v), using Equation (6) [37], shows that for the MoO_3 and $MASnBr_3$ HTL materials, an energy spike ($\Delta E_v > 0$) is formed at the Sb_2S_3/HTL interface. In this case, the activation energy (E_a) (Table 6) for the carrier recombination is equal to the bandgap energy of the Sb_2S_3 absorber [53]. Furthermore, based on the hole mobility (Table 5) and conduction band offset (ΔE_c) at the Sb_2S_3/MoO_3 HTL and Sb_2S_3/$MASnBr_3$ HTL interfaces (Table 6), the simulated solar cell efficiencies are classified as follows: MoO_3> $MASnBr_3$ (Table 6). These results show a relationship between the activation energy, ΔE_c, at the absorber/HTL interface and the simulated efficiency when $\Delta E_v > 0$. On the other hand, $\Delta E_v < 0$ for Cu_2O, CuI, and CuSCN HTL materials, indicating the formation of an energy cliff at the absorber/HTL interface; and E_a (Equation (7) [48]) for carrier recombination becomes lower than the absorber bandgap. This energy cliff does not impede the flow of the

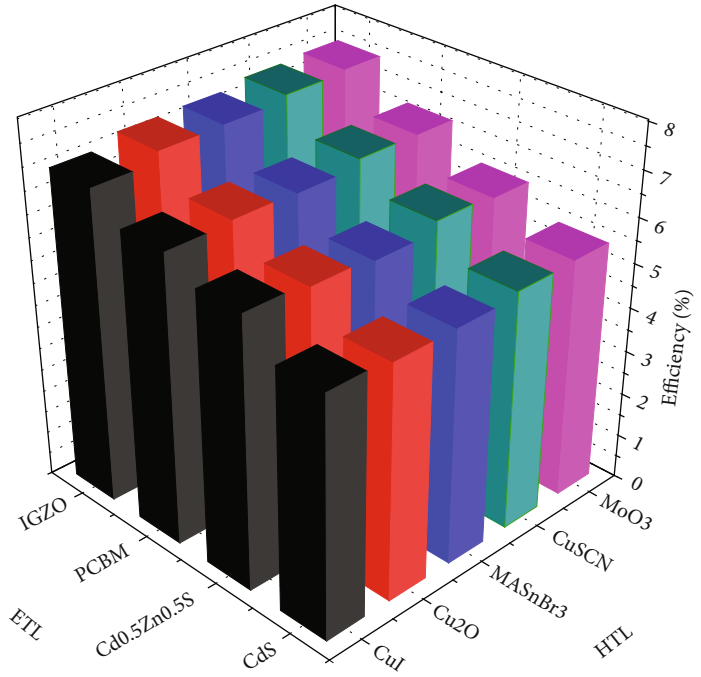

Figure 4: Impact of different ETL-HTL material combinations on the efficiency of Sb_2S_3 solar cell.

holes. In the case of CuSCN HTL, the large conduction band offset formed at the Sb_2S_3/CuSCN HTL interface (Table 6) acts as an electron blocker. It prevents electrons from flowing from the absorber to the HTL layer to recombine with holes. This could justify that CuSCN HTL presents the second-best efficiency, after that of MoO_3 HTL. E_a values for CuO_2 and CuI HTL materials are 1.67 eV and 1.5 eV, respectively, and simulated efficiencies are CuO_2> CuI (Table 6). This is due to the hole mobility of CuO_2 HTL (80 cm^2/Vs), which is much higher than that of CuI HTL (43.9 cm^2/Vs) and to the highest negative VBO for CuI HTL.

The effect of different HTL materials shows that a HTL with both an energy spike at the Sb_2S_3/HTL interface and high hole mobility achieves better solar cell efficiency. These properties are the reason why MoO_3 is chosen as the best HTL material for the rest of the Sb_2S_3-based solar cell optimization process.

$$\Delta E_v = \chi_{\_HTL} - \chi_{\_Sb_2S_3} + E_{g\_HTL} - E_{g\_Sb_2S_3}, \quad (6)$$

$$E_a = E_{g\_Sb_2S_3} - |\Delta E_v|. \quad (7)$$

The effect of the operating temperature on the electrical parameters of the initial solar cell (Figure 1(a)) and the FTO/(ZnO/IGZO)/Sb_2S_3/MoO_3/Au solar cell is shown in Figure S4. This allows us to discuss the thermal stability of these solar cells when the temperature is varied from 300 K to 390 K. In both cases, it can be seen that the electrical parameters decrease with increasing temperature. The thermal coefficient (TC) of the electrical parameters of each solar cell (Figure S4) shows that our proposed FTO/(ZnO/IGZO)/Sb_2S_3/MoO_3/Au solar cell, with a TC of -0.35%/K for efficiency, is more stable than the initial solar cell (Figure 1(a)), with a TC of -0.53%/K for efficiency. This result further justifies the need to replace Spiro-OMeTAD HTL to improve solar cell thermal stability. Therefore, the FTO/(ZnO/IGZO)/Sb_2S_3/MoO_3/Au solar cell, where *h*-ETL is ZnO/IGZO, will be further optimized to improve its performance in the remainder of this work.

3.4. Design of High-Efficiency FTO/(ZnO/IGZO)/Sb_2S_3/MoO_3/Au Solar Cell. Optimization of a solar cell is the process of determining the parameters where the cell is most efficient. This process is the study of the influence of certain parameters of the layers of the solar cell on the performance of the device. Thus, at the end of each study, the value of the parameter that gives the best solar cell performance is retained and used in the next study.

3.4.1. Optimization of the Sb_2S_3 Absorber Layer

(1) Influence of Sb_2S_3 Absorber Layer Thickness. The thickness of the absorber is an essential parameter in optimizing the performance of solar cells. It regulates photon absorption, charge generation, and recombination mechanisms. Figure 6 shows the evolution of the simulated solar cell performance parameters as the Sb_2S_3 absorber thickness varies from 0.15 μm to 0.35 μm. The other parameters are kept constant according to Tables 1, 3, and 5. It can be seen that J_{SC}, V_{OC}, and efficiency increase with increasing absorber thickness (Figures 6(a) and 6(b)). The increase in these electrical parameters can be explained by the fact that as the absorber thickness increases, more photons with longer wavelengths are absorbed. This favors the generation of a larger number of electron-hole pairs due to the high absorption of the Sb_2S_3 absorber [59]. The increased V_{OC} with absorber thickness could also be attributed to improved p-n junction quality [60]. However, with an optimum thickness of 0.28 μm, a maximum efficiency of 7.83% is achieved. Beyond this Sb_2S_3 absorber thickness, the efficiency starts to

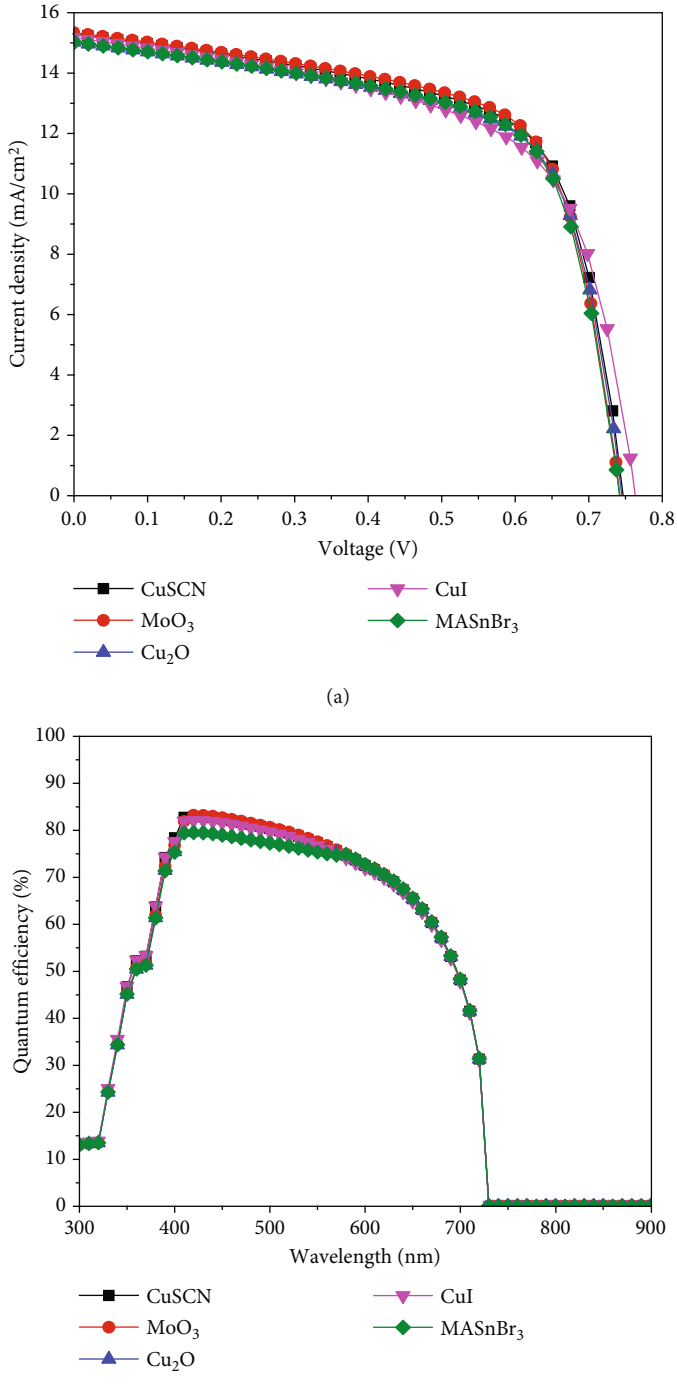

Figure 5: Effect of different HTL materials on (a) J-V characteristics and (b) quantum efficiency of a Sb_2S_3-based solar cell.

decrease as shown in Figure 6(b). The reason for this decrease is mainly due to the strong recombination of photogenerated electrons deep inside the absorber. Due to the very short electron diffusion length in the Sb_2S_3 absorber, these electrons recombine before reaching the ETL/Sb_2S_3 interface [61]. On the other hand, an increase in absorber thickness also results in a decrease in the fill factor (FF) of the solar cell (Figure 6(b)). The increase in series resistance with absorber thickness is responsible for this reduction in FF [62]. For the rest of our simulations, we set the Sb_2S_3 absorber thickness to 0.28 μm.

(2) Influence of Bulk Defect Density of the Sb_2S_3 Absorber. The bulk defect density (N_t) in the absorber layer is also an essential factor affecting solar cell performance. It is essential to understand how this affects performance. Figure 7 shows the influence of the bulk defect density of the Sb_2S_3 absorber layer on the simulated solar cell

Table 6: Simulated performance parameters, VBO, and activation energy of a Sb_2S_3-based solar cell using different HTL materials.

	Electrical parameters						
HTL	J_{SC} (mA/cm^2)	V_{OC} (V)	FF (%)	η (%)	ΔE_c (eV)	ΔE_v (eV)	E_a (eV)
MoO_3	15.33	0.74	65.31	7.44	1.2	0.1	1.7
CuSCN	15.29	0.74	64.54	7.39	2	-0.1	1.6
$MASnBr_3$	15.02	0.74	65.09	7.26	0.31	0.14	1.7
Cu_2O	15.02	0.74	64.56	7.24	0.5	-0.03	1.67
CuI	15.17	0.76	60.59	7.03	1.6	-0.2	1.5

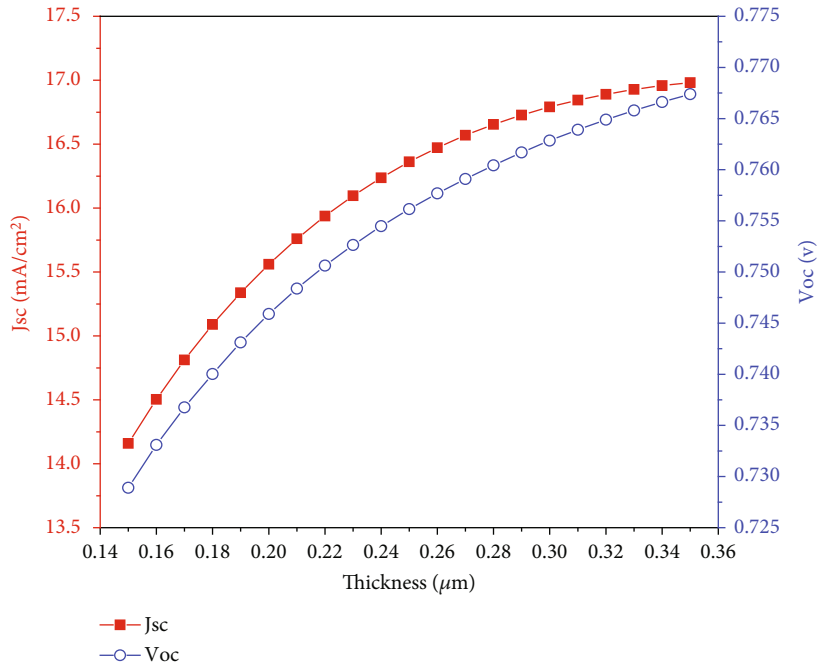

(a)

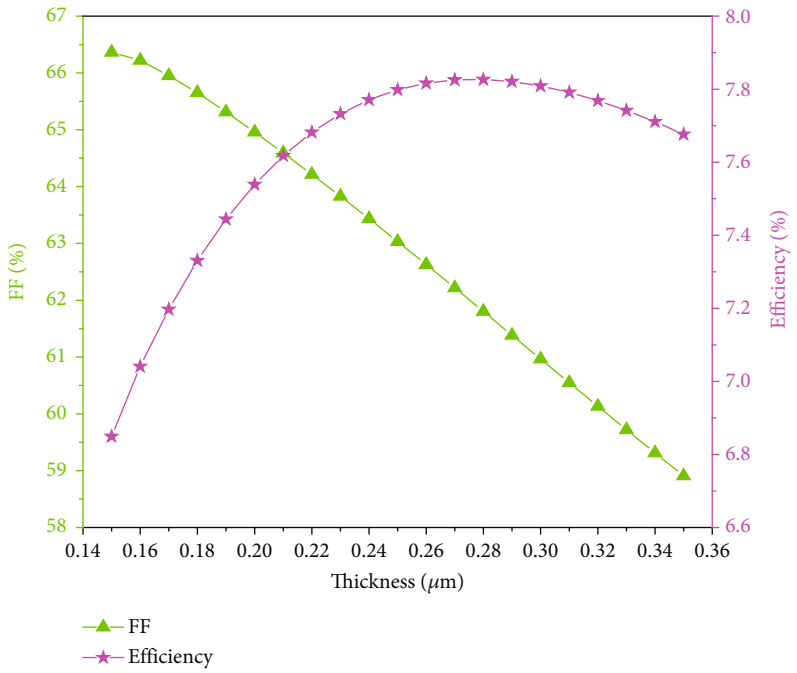

(b)

Figure 6: Solar cell performance versus Sb_2S_3 absorber thickness: (a) J_{SC} and V_{OC} and (b) FF and efficiency.

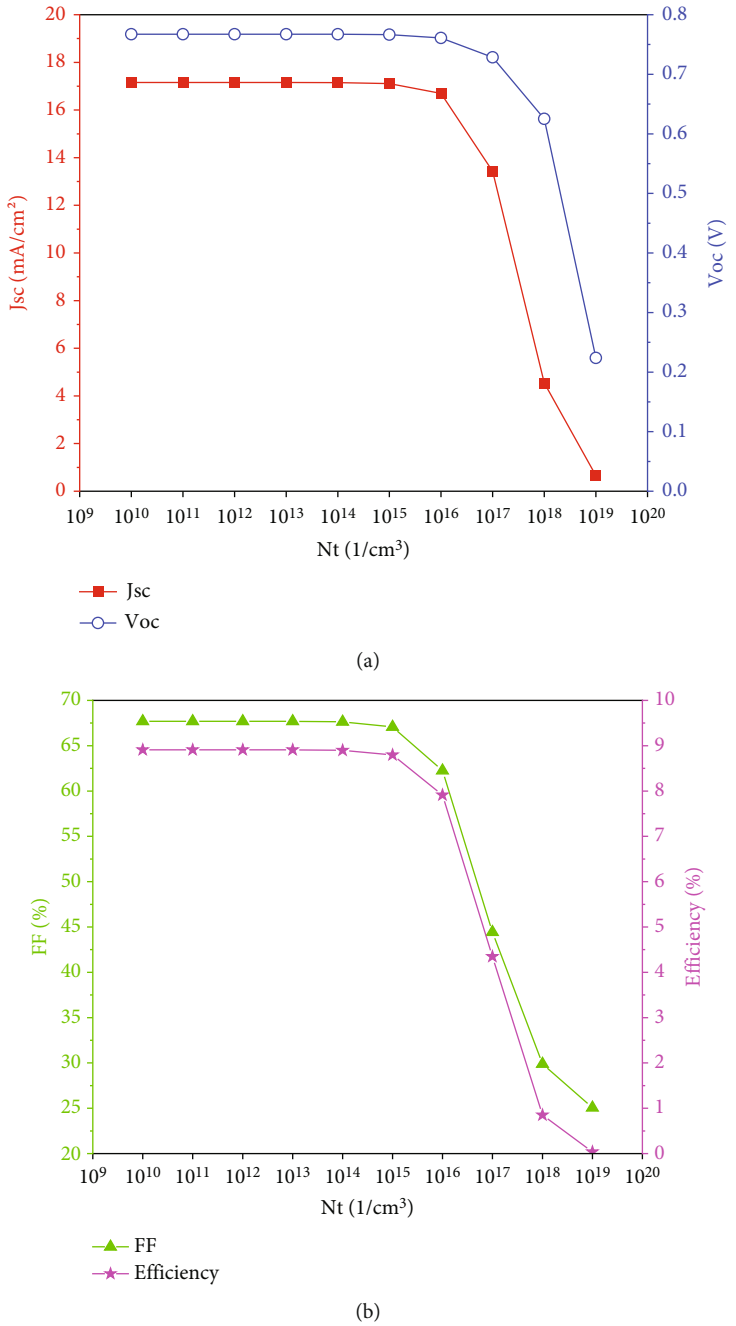

Figure 7: Variation of solar cell electrical parameters as a function of absorber bulk defect density: (a) J_{SC} and V_{OC} and (b) FF and efficiency.

performance (J_{SC}, V_{OC}, FF, and efficiency). It varies in the range from $10^{10}\,cm^{-3}$ to $10^{19}\,cm^{-3}$. The analysis of the results obtained reveals two trends: (i) on the one hand, the performance parameters vary very little when the bulk defect density is between $10^{10}\,cm^{-3}$ and $10^{15}\,cm^{-3}$, and (ii) on the other hand, decreasing sharply for defect densities above $10^{15}\,cm^{-3}$ (Figures 7(a) and 7(b)). In fact, the efficiency goes from 8.91% at $10^{10}\,cm^{-3}$ bulk defect density to 0.04% at $10^{19}\,cm^{-3}$ bulk defect density (Figure 7(b)). Equations (8) and (9) [42, 50] show that an increase of the bulk defect density (N_t) leads to a decrease of the carrier lifetime and thus to a decrease of their diffusion length (Equation (10) [42, 50]), which leads to an increase in the absorber recombination rate [62]. The results show that Sb_2S_3-based solar cells perform best when the absorber bulk defect density is less than $10^{15}\,cm^{-3}$. Therefore, in this study, we choose a bulk defect density of $10^{10}\,cm^{-3}$ for the Sb_2S_3 absorber for our further work. These results are in good agreement with those obtained by Odari et al. [40].

$$\tau_n = \frac{1}{\sigma_n \nu_{th} N_t}, \tag{8}$$

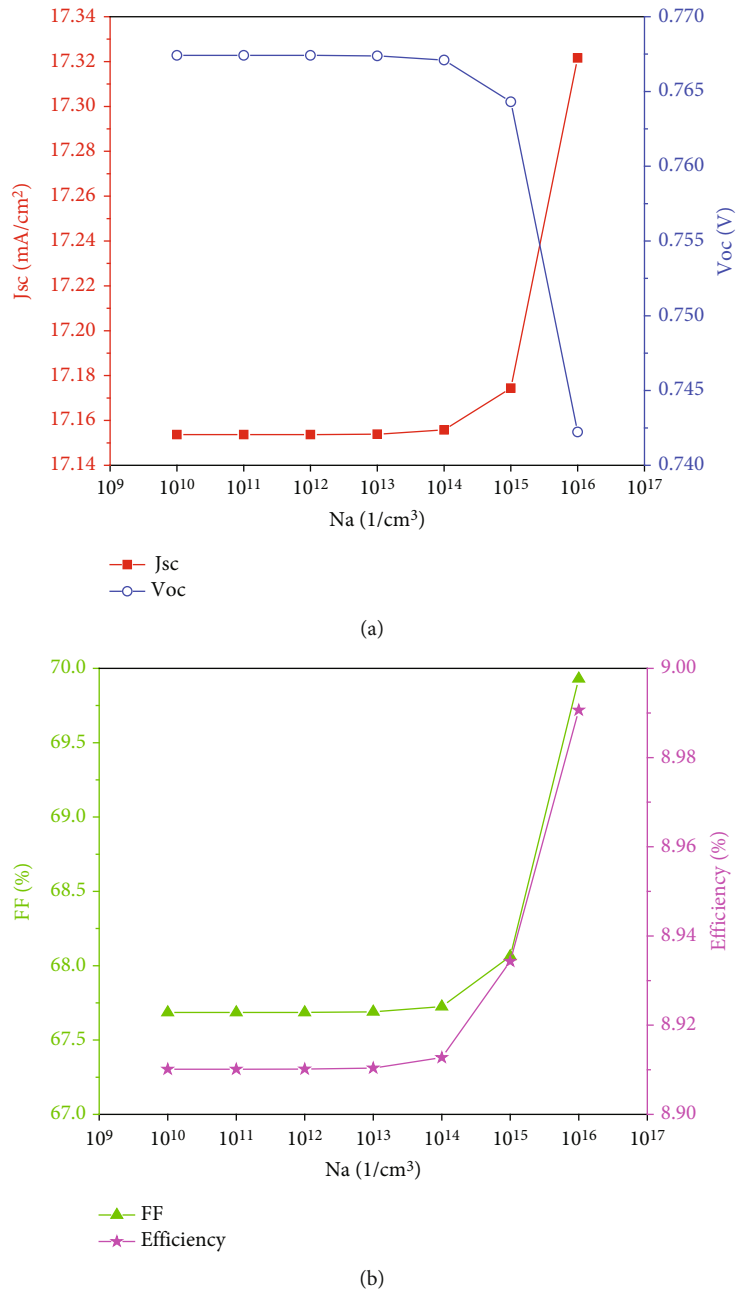

FIGURE 8: Influence of variation of the acceptor concentration in the Sb_2S_3 layer on the electrical parameters: (a) J_{SC} and V_{OC} and (b) FF and efficiency.

$$\tau_p = \frac{1}{\sigma_p \nu_{th} N_t}, \tag{9}$$

$$l = \sqrt{D\tau}, \text{ with } D = \frac{\mu KT}{q}. \tag{10}$$

(3) Influence of the Acceptor Concentration of the Sb_2S_3 Absorber. To evaluate the effect of the Sb_2S_3 absorber acceptor concentration (N_A) on the solar cell performance (J_{SC}, V_{OC}, FF, and efficiency), a variation from $10^{10}\,cm^{-3}$ to $10^{16}\,cm^{-3}$ was performed; the results are shown in Figures 8(a) and 8(b). The performance parameters show almost constant values when the N_A concentration is less than or equal to $10^{14}\,cm^{-3}$. Above this value, the performance increases, except for V_{OC} (Figure 8(a)), which decreases with increasing N_A concentration; this would be associated with a shift of the Fermi levels towards the center of the bandgap and would facilitate the excitation of the charge [40]. These results are in agreement with those of Odari et al. [40]. Increasing N_A reduces the trapping of photogenerated charges in the Sb_2S_3 absorber layer and thus improves their collection [40]. A maximum efficiency of 8.99% is obtained for an absorber acceptor concentration of $10^{16}\,cm^{-3}$. Thus, we set the doping of the Sb_2S_3 absorber layer at $10^{16}\,cm^{-3}$.

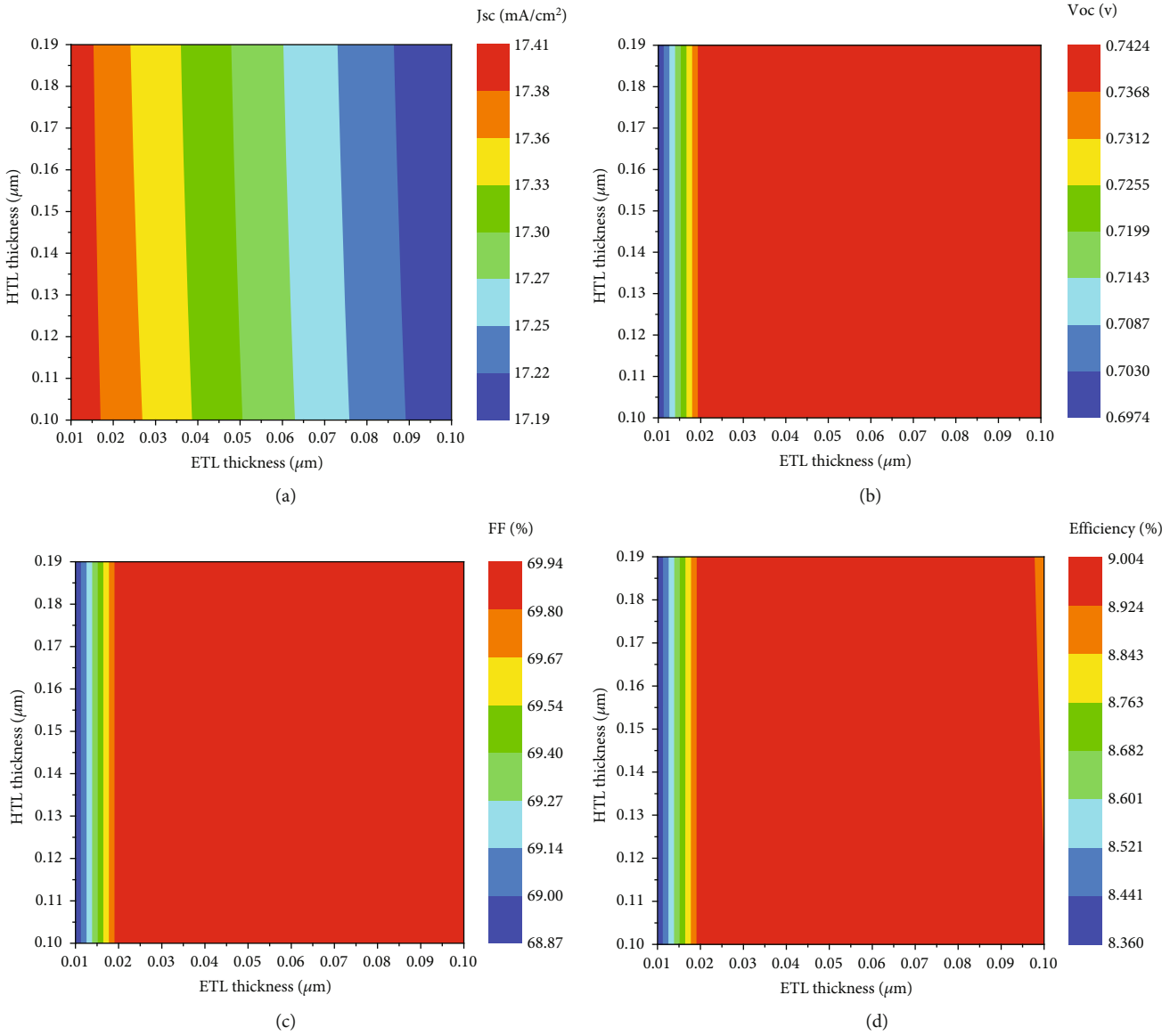

Figure 9: Contour plot of Sb_2S_3-based solar cell electrical parameters as a function of the thickness of the IGZO ETL and MoO_3 HTL materials: (a) J_{SC}, (b) V_{OC}, (c) FF, and (d) efficiency.

3.4.2. Optimization of ETL and HTL Layer Thicknesses. The focus of this section is on the influence of the thickness of the IGZO ETL and MoO_3 HTL materials. Thus, the thicknesses of the IGZO ETL and MoO_3 HTL layers vary simultaneously in the range of 0.01 μm to 0.1 μm and 0.1 μm to 0.19 μm, respectively, under the consideration of the previously optimized parameters. Figure 9 shows that the MoO_3 HTL thickness has no effect on the solar cell performance, regardless of the IGZO ETL thickness. The reason is that this layer does not affect the generation and recombination processes in the absorber layer. This result is in agreement with the results of Gamal et al. [63]. The thickness of the ETL layer greatly affects the electrical parameters of the solar cell. J_{SC} decreases with increasing ETL thickness (Figure 9(a)), as fewer photons reach the absorber layer, reducing the photocurrent and J_{SC}. On the contrary, a thicker ETL layer increases the space charge region width, which induces an increase in the electric field at the ETL/absorber interface, thus allowing good carrier separation at this interface. Hence, there is an increase in V_{OC} (reduction in surface recombination) (Figure 9(b)), FF (Figure 9(c)), and efficiency (Figure 9(d)). This study shows that HTL thickness has no effect on solar cell performance; conversely, thicker ETL increases the width of the space charge region, which causes an increase in electric field at the ETL/absorber interface. For IGZO ETL and MoO_3 HTL thicknesses of 0.03 μm and 0.1 μm, respectively, the solar cell achieves an efficiency of 9.00% (J_{SC} = 17.32 mA/cm^2, V_{OC} = 0.7422 V, and FF = 69.93%).

3.4.3. Influence of IGZO/Sb_2S_3 Interface Defect Density on Solar Cell Electrical Parameters. The quality of the metallurgical interface also affects the productivity of a solar cell. In

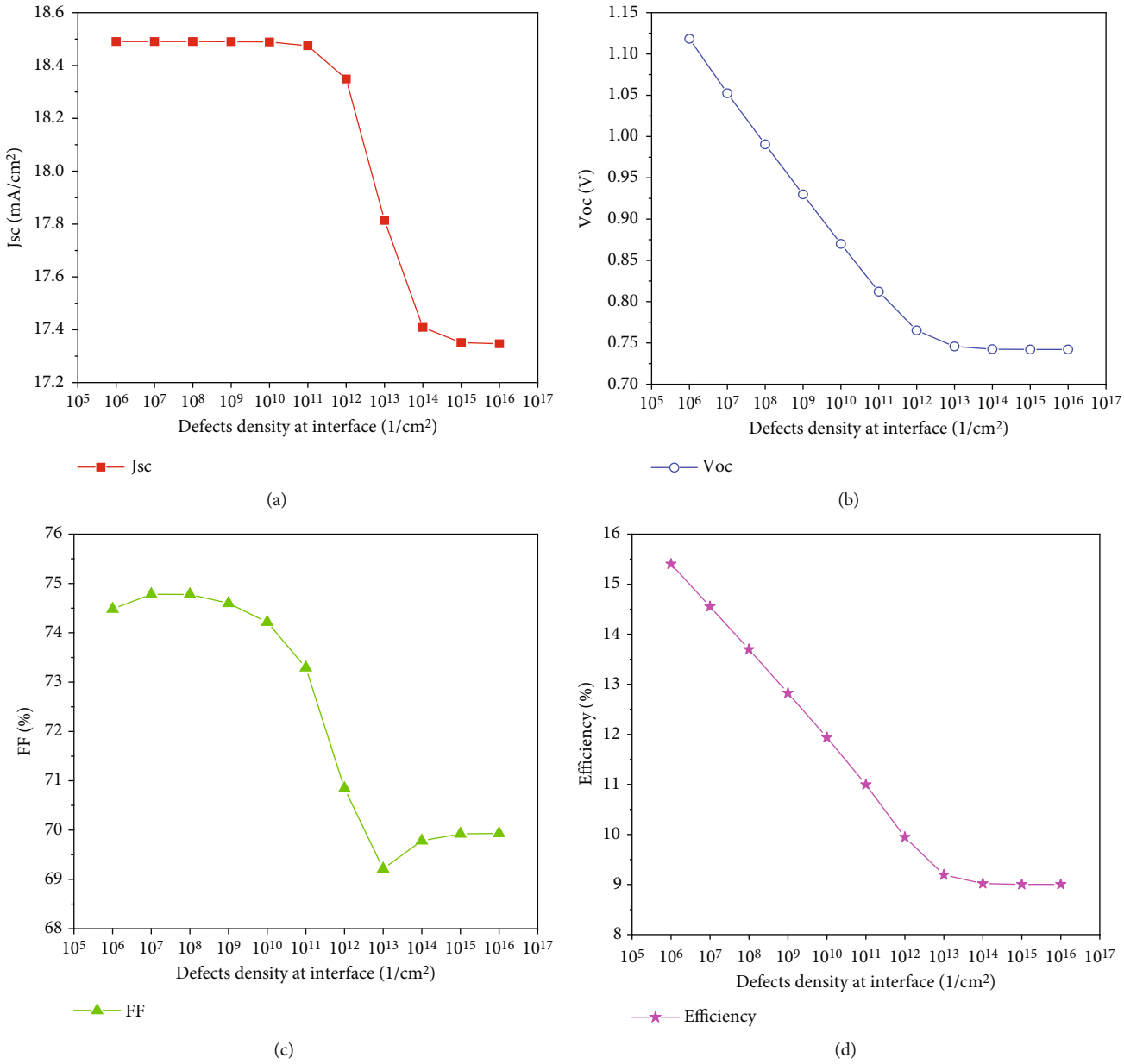

FIGURE 10: Variation of Sb_2S_3 solar cell electrical parameters as a function of IGZO/Sb_2S_3 interface defect density: (a) J_{SC}, (b) V_{OC}, (c) FF, and (d) efficiency.

this subsection, the effect of defect density at the IGZO/Sb_2S_3 interface on device performance is investigated. This defect density is varied from $10^6\,cm^{-2}$ to $10^{16}\,cm^{-2}$. Figure 10 depicts the evolution of the simulated electrical parameters (J_{SC}, V_{OC}, FF, and efficiency) as a function of the defect density at the IGZO/Sb_2S_3 interface. The results clearly show that the defect density at the metallurgical junction ETL/absorber interface significantly affects the solar cell performance. In indeed, the short-circuit current density (J_{SC}) remains stable (around $18.4\,mA/cm^2$) for defect densities in the range of $10^6\,cm^{-2}$ to $10^{11}\,cm^{-2}$ (Figure 10(a)). Above $10^{11}\,cm^{-2}$, the defect density increases the carrier recombination rate at this interface. This leads to a rapid decrease of the J_{SC} [64]. This increase in the rate of carrier recombination at the interface is also responsible for the rapid decrease in V_{OC} [65], as shown in Figure 10(b). The fill factor (FF) decreases from 74.48 to 69.21% (Figure 10(c)). This is due to the high heterojunction resistance of the solar cell, caused by the increased defect density at the main junction interface [65]. It then increases slightly when the defect density exceeds $10^{13}\,cm^{-2}$. Due to its dependence on J_{SC}, V_{OC}, and FF, the solar cell efficiency (Equation (11) [66]) is also affected by this defect density variation at the main junction interface. Indeed, solar cell efficiency drops from 15.40% to 9.00% as main junction defect density increases (Figure 10(d)). Xiao et al. [15] considered a value of $10^9\,cm^{-2}$ for the defect density at the ETL/Sb_2S_3 and Sb_2S_3/HTL interfaces in their simulation work. The defect

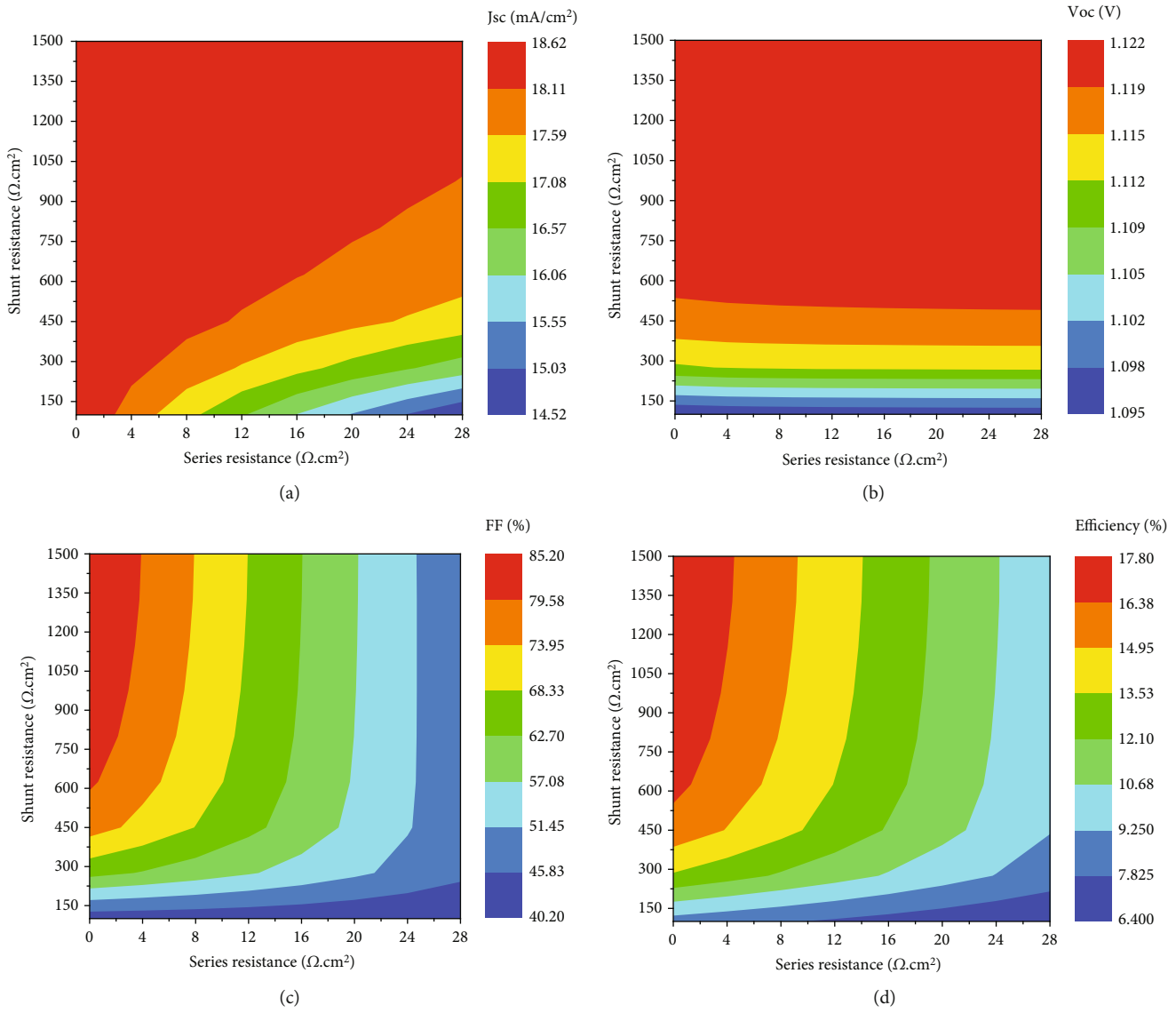

FIGURE 11: Contour plot of solar cell electrical parameters as a function of series resistance (R_S) and shunt resistance (R_{SH}): (a) J_{SC}, (b) V_{OC}, (c) FF, and (d) efficiency.

density at the ETL/Sb_2S_3 interface is set to $10^6\,cm^{-2}$ for further simulations.

$$\eta = \frac{P_{max}}{P_{in}} = \frac{FF \cdot J_{sc} \cdot V_{oc}}{P_{in}}. \quad (11)$$

3.4.4. Influence of Series and Shunt Resistances on Device Performance. Series resistance (R_S) and shunt resistance (R_{SH}) have a significant impact on solar cell performance. R_S is a combination of several resistances, including those associated with the interface between the layers and the metal contacts (the front and back contacts). It also includes those encountered by the current flowing through the emitter and base of the solar cell. In contrast, R_{SH} is caused by leakage current [65]. The effect of varying R_S and R_{SH} in the ranges 0-28 $\Omega{\cdot}cm^2$ and 100-1500 $\Omega{\cdot}cm^2$, respectively, on the simulated performance parameters (J_{SC}, V_{OC}, FF, and efficiency) of the device is depicted in Figure 11. For a fixed value of R_{SH}, J_{SC} decreases as R_S increases (Figure 11(a)) due to an increase in internal resistance. This impedes the transport of charge carriers to the electrodes [67]. Conversely, J_{SC} increases as R_{SH} increases for a fixed value of R_S. Figure 11(b) shows that R_S has no significant effect on V_{OC}. On the contrary, an increase in R_{SH} leads to a slight increase in the open-circuit voltage. Indeed, increasing R_{SH} reduces the saturation current J_0, which increases V_{OC} (Equation (12) [68, 69]).

$$V_{OC} = \frac{nK_BT}{q} \ln\left[\frac{J_{SC}}{J_0} + 1\right]. \quad (12)$$

Figure 11(a) shows that FF decreases as R_S increases. This is consistent with Equation (13) [70]. In reverse, the increase in FF with the resistance R_{SH} is due to low recombination rates [71].

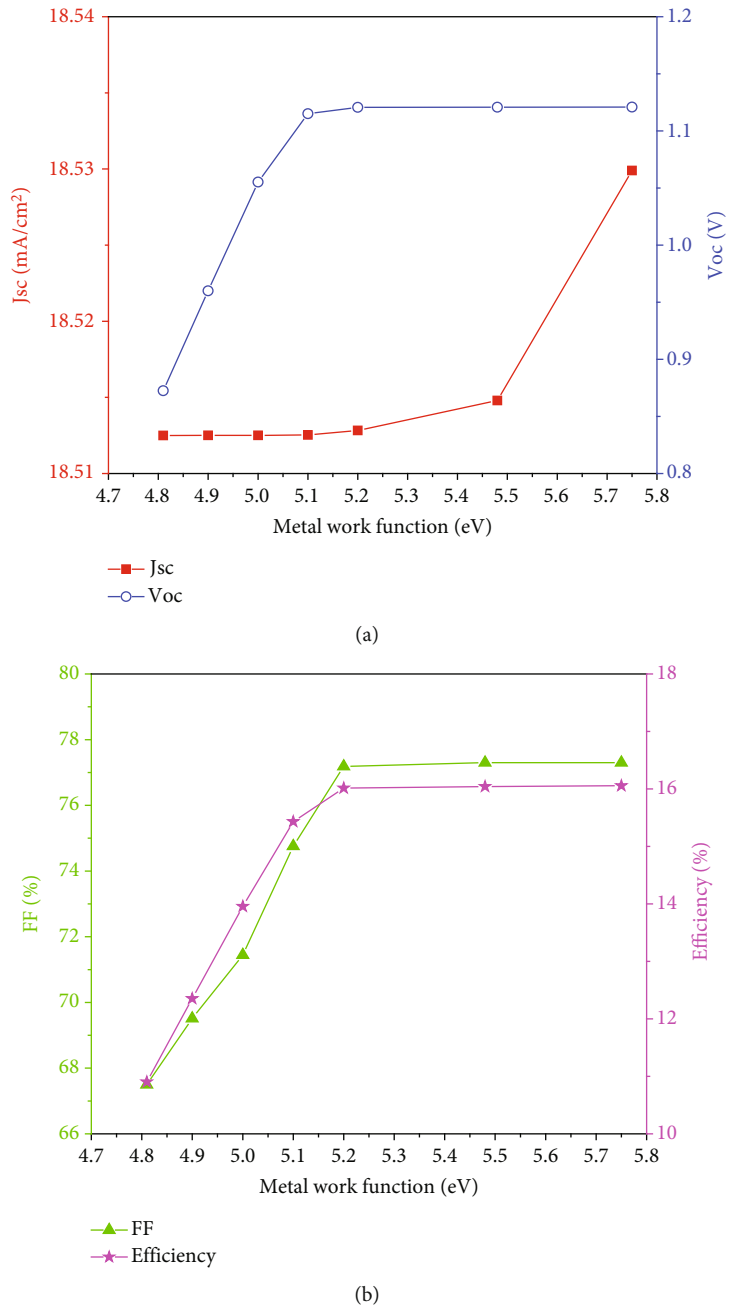

FIGURE 12: Evolution of Sb_2S_3 solar cell electrical parameters as a function of metal work function: (a) J_{SC} and V_{OC} and (b) FF and efficiency.

$$\mathrm{FF} = \mathrm{FF}_{\mathrm{ref}}\left(1 - R_s \frac{J_{SC}}{V_{OC}}\right), \tag{13}$$

where $\mathrm{FF}_{\mathrm{ref}}$ is the reference fill factor of the solar cell for a given R_S.

Solar cell conversion efficiency (Figure 11(d)) follows the same trend as the fill factor (Figure 11(c)). It can be seen that increasing R_S negatively affects solar cell efficiency, while increasing R_{SH} significantly increases the efficiency (positive effect). These simulation results show that when designing solar cells, the layers should be arranged to minimize R_S and maximize R_{SH}. The experimental results show that the R_S and R_{SH} values of Sb_2S_3-based solar cells are in the ranges of 4.71-40 $\Omega\cdot\mathrm{cm}^2$ and 49.9-856.35 $\Omega\cdot\mathrm{cm}^2$, respectively [12]. The optimum values of R_S and R_{SH} are set at 4 $\Omega\cdot\mathrm{cm}^2$ and 800 $\Omega\cdot\mathrm{cm}^2$, respectively, for this simulation.

3.4.5. Effect of Rear Contact Extraction Energy and Operating Temperature. Another important factor in improving the efficiency of a solar cell is the metal work function (MWF) or the extraction energy of the back contact. To study the effect of this energy on the performance of the simulated

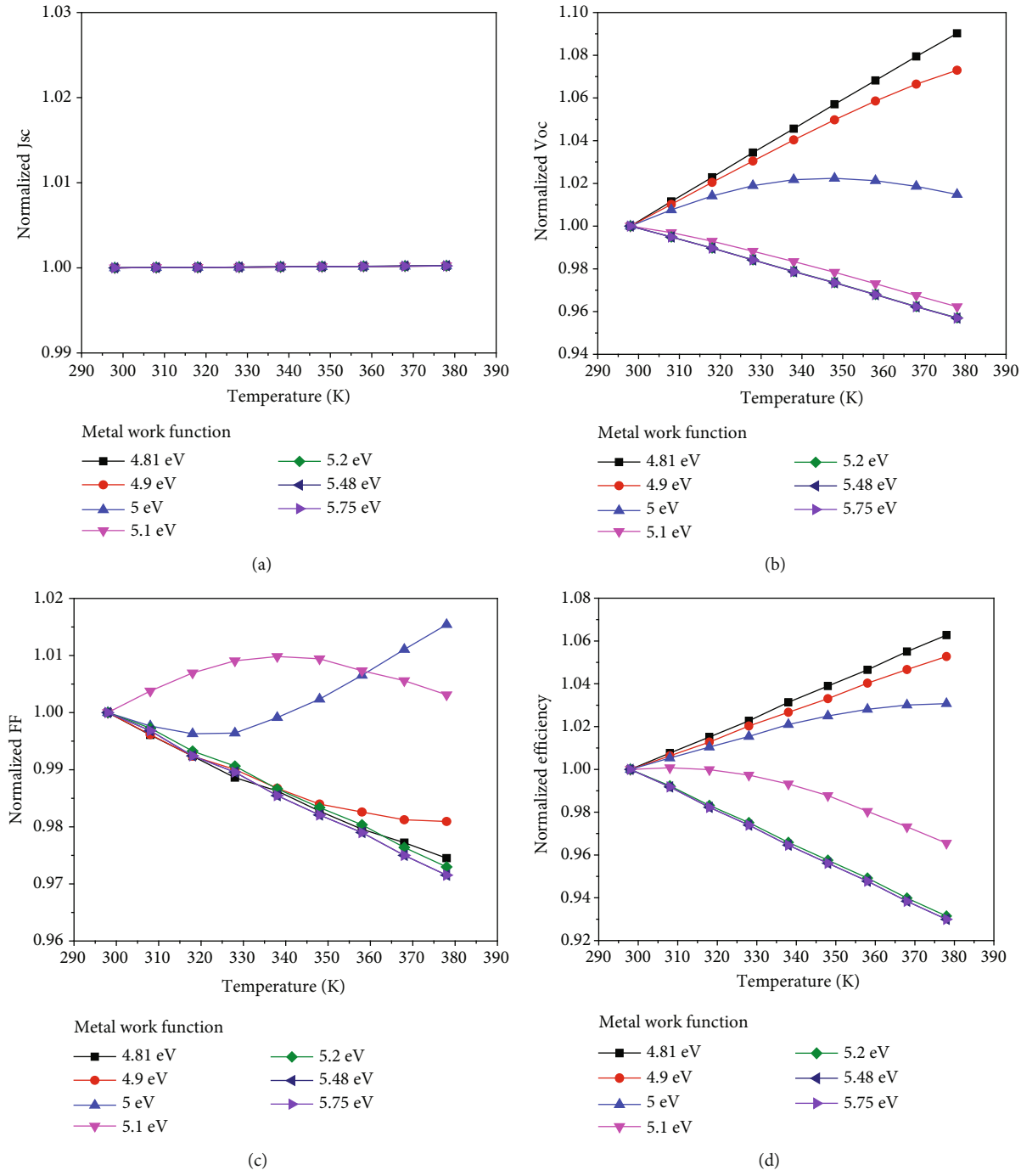

FIGURE 13: Normalized electrical parameters of a Sb_2S_3 solar cell as a function of the operating temperature for different types of rear metal contacts: (a) J_{SC}, (b) V_{OC}, (c) FF, and (d) efficiency.

solar cell, several back contacts such as iron (Fe), copper (Cu), molybdenum (Mo), nickel (Ni), gold (Au), palladium (Pd), and platinum (Pt) were tested, all derived from the work of Derry et al. [72]. Figures 12(a) and 12(b)show that the solar cell electrical parameters increase with increasing extraction energy. Indeed, increasing the extraction energy decreases the potential barrier φ_b (Equation (14) [39]) at the HTL/back contact interface, leading to improved solar cell electrical parameters (Table S5).

$$\varphi_b = E_g + \chi - \varphi_m, \tag{14}$$

where E_g and χ are the HTL bandgap and electron affinity, respectively, and φ_m is back contact extraction energy.

In order to combine thermal stability and high performance in the selection of the best back contact, we also evaluate the operating temperature effect on solar cell performance for these previous back contacts. In fact,

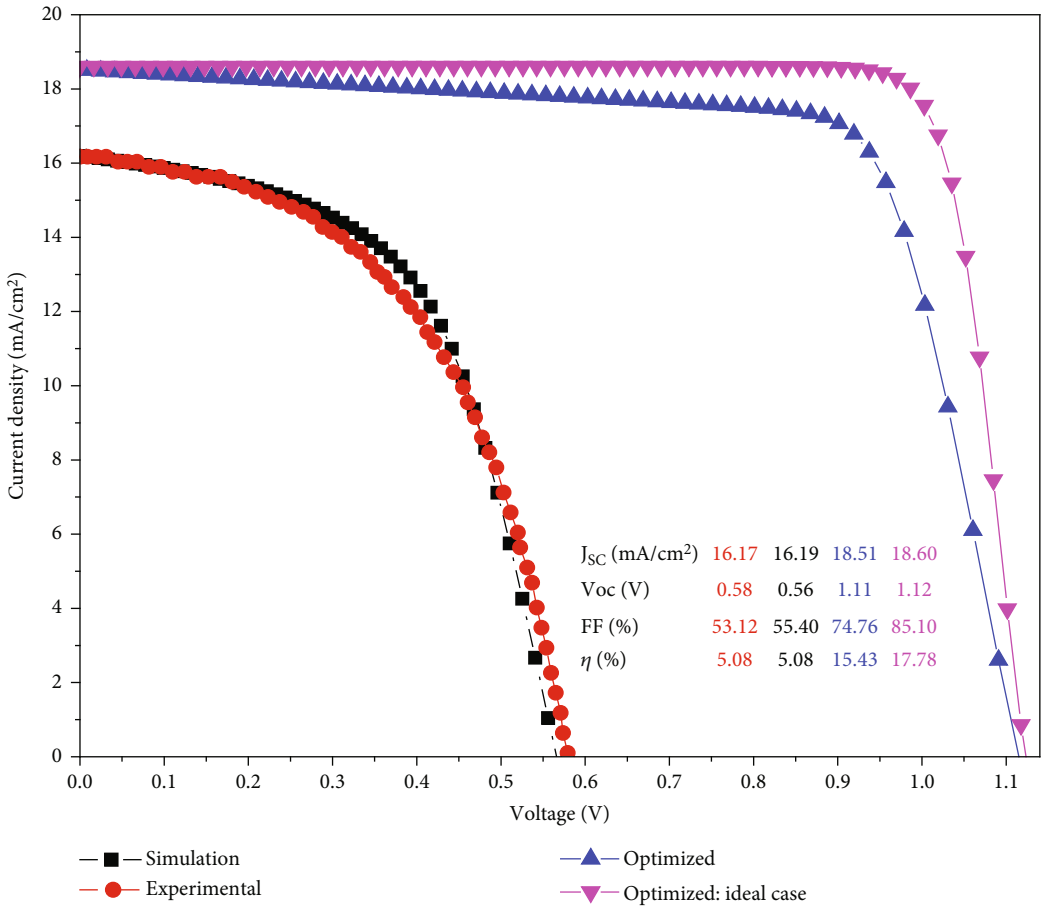

Figure 14: J-V characteristics of experiment (red), simulation (black), optimization (blue), and idealized (pink) structures.

Table 7: Optimized parameters of the Sb_2S_3 solar cell.

Optimized parameters	Values
Absorber thickness	0.28 μm
Absorber bulk defect density	10^{10} cm^{-3}
Absorber acceptor concentration	10^{16} cm^{-3}
Thickness of IGZO ELT and MoO_3 HTL materials	0.03 μm and 0.1 μm
IGZO/Sb_2S_3 interface defect density	10^{6} cm^{-2}
R_S and R_{SH} resistances	4 Ω·cm^2 and 800 Ω·cm^2
Back contact extraction energy (nickel)	5.1 eV

Table 8: Electrical parameters of experimental, simulated, and optimized solar cells.

Solar cell	J_{SC} (mA/cm^2)	V_{OC} (V)	FF (%)	η (%)
Experimental	16.17	0.58	53.12	5.08
Simulated	16.19	0.56	55.40	5.08
Optimized	18.51	1.11	74.76	15.43

operating temperature is an essential parameter in solar cell design. Figure 13 depicts the effect of operating temperature, which ranges from 298 K to 378 K (25°C to 105°C), on solar cell electrical parameters for different contacts.

The short-circuit current density (J_{SC}) is not sensitive to the temperature gradient and the extraction energy of the back contact (Figure 13(a)). In fact, the J_{SC} is proportional to the number of photogenerated carriers, which increases with temperature [73]. However, the more photogenerated carriers, the more collisions occur, increasing the probability of recombination. These opposing phenomena tend to keep the J_{SC} constant [74]. These results are consistent with those reported by Abena et al. [37] and Jhuma et al. [74].

On the one hand, Figure 13(b) shows that when the extraction energy is greater than or equal to 5.1 eV, the V_{OC} decreases linearly with increasing operating temperature. This decrease is due to the fact that the saturation current J_0 (Equation (15) [66]) increases with temperature, which reduces the V_{OC} (Equation (12)). On the other hand, when φ_m is less than 5.1 eV, the V_{OC} increases with the temperature gradient and the decrease in the metal work function. Indeed, as the temperature increases, the bandgap decreases (Equation (16) [68]), which reduces the recombination current (Equation (15)) and induces the increase in V_{OC} (Equation (12)). Furthermore, the low metal work function (less than 5.1 eV) induces low potential barriers, which allows good carrier collection.

Table 9: Performance parameters of Sb_2S_3-based solar cells reported in the literature and those obtained in this work.

Search type	Proposed cell structure	J_{SC} (mA/cm^2)	V_{OC} (V)	FF (%)	η (%)
Experimental	FTO/(ZnO/TiO_2)/Sb_2S_3 (E_g = 1.7 eV)/Spiro-OMeTAD/Au [23]	16.17	0.58	53.12	5.08
	ITO/CdS/Sb_2S_3 (E_g = 1.7 eV)/Au [76]	10.8	0.71	45.5	3.5
	FTO/CdS/Sb_2S_3 (E_g = 1.7 eV/Au [77]	10.92	0.588	46.77	3.01
	FTO/CdS/Sb_2S_3 (E_g = 1.61 eV)/Au [78]	9.14	0.54	47.48	2.20
	SLG/Mo/Sb_2S_3 (E_g = 1.75 eV)/Cds/i-ZO/AZO/Ni:Al [79]	5.96	0.574	37.78	1.29
Simulation	FTO/ZnS/Sb_2S_3 (E_g = 1.62 eV)/Cu_2O/Au [15]	24.41	1.111	84.04	22.78
	FTO/CdZnS/Sb_2S_3/carbon [16]	21.99	1.192	85.37	22.39
	FTO/TiO_2/Sb_2S_3 (E_g = 1.7 eV)/Cu_2O/Au [75]	24.44	0.948	79.96	21.43
	AZO/ZnO/CdS/Sb_2S_3 (E_g = 1.62 eV)/Au [13]	20.15	1.23	83.1	20.60
	CdS/Sb_2S_3 (E_g = 1.62 eV)/Pt [14]	19.04	1.31	85.90	18.52
	ZnO:Al/i-ZnO/CdS/Sb_2S_3 (E_g = 1.62 eV)/Mo [12]	15.98	0.723	83.23	9.51
	Glass/TCO/TiO_2/Sb_2S_3 (E_g = 1.7 eV)/P3HT/Ag [40]	15.23	0.75	73.55	8.41
	Glass/FTO/(ZnO/IGZO)/Sb_2S_3 (E_g = 1.7 eV)/MoO_3/Ni (this work)	18.51	1.11	74.76	15.43
	Ideal case (R_S = 0 Ω·cm^2; R_{SH} = ∞) (this work)	18.60	1.12	85.10	17.73

$$J_0 = A \times \exp\left(-\frac{qE_g}{k_B T}\right), \tag{15}$$

where $A = 1.5 \times 10^8$ mA/cm^2.

$$E_g(T) = E_g(0) - \frac{\alpha \cdot T^2}{(T+\beta)}, \tag{16}$$

where $E_g(T)$ is the bandgap, T is the absolute temperature, $E_g(0)$ is the bandgap at $T \approx 0$ K, and α and β are the constants that characterize the semiconductor material.

Figure 13(c) shows that the fill factor (FF) decreases with increasing temperature. However, this trend is not followed by devices with metal work functions of 5 eV and 5.1 eV. This can be explained by the fact that at these values, less recombination is generated in the device and therefore does not cause the FF to decrease.

The evolution of solar cell efficiency (Figure 13(d)) is imposed by V_{OC} (Figure 13(b)), since both curves follow the same trend. In addition, the temperature-dependent efficiency of each device shows that there are three ranges of thermal stability for the different back contacts used (Table S6):

(i) The first range corresponds to devices with a back contact extraction energy below 5.1 eV. These devices are characterized by good thermal stability

(ii) The second is devices with extraction energies above 5.1 eV. These are devices with low thermal stability

(iii) The devices with MWF of 5.1 eV are the third series. The thermal stability of this series is intermediate between the two previous series

Therefore, based on the above analysis, we conclude that the Sb_2S_3-based solar cell that combines high performance (15.43%) and the best thermal stability (-0.043%/K) is the structure with the back contact extraction energy of 5.1 eV (Table S6).

3.4.6. Optimized Solar Cell Structure and Comparison. Figure 14 shows the *J-V* characteristics of the Sb_2S_3-based solar cell experimentally reported by Baron Jaimes et al. [23], the one we simulated using the SCAPS-1D software for model validation, the one optimized by simulation considering the optimal parameters obtained in the previous sections (Table 7), and the one for the ideal case (when R_S is neglected and R_{SH} is very large). Table 8 summarizes the electrical parameters of the different structures and shows how the performance differs. As a result, the efficiency of the Sb_2S_3-based solar cell increased from 5.08% (J_{SC} = 16.19 mA/cm^2, V_{OC} = 0.56 V, and FF = 55.40%) to 15.43% (J_{SC} = 18.51 mA/cm^2, V_{OC} = 1.11 V, and FF = 74.76%). Furthermore, to compare our results, some performance parameters of Sb_2S_3 solar cells reported in the literature are shown in Table 9. The performance of the solar cell is affected by a small change in the Sb_2S_3 absorber bandgap. It should be noted that the devices with a Sb_2S_3 absorber bandgap of 1.7 eV, e.g., the work of Chen et al. [75], show a considerable difference. This can be due to different configurations (interfaces, resistors, etc.), optimization parameters, and the optimization process.

4. Conclusion

In this work, the experimental Sb_2S_3-based solar cell, with hybrid electron transport layer (ZnO/TiO_2), was designed and simulated using SCAPS-1D software. To solve the stability problems of using the Spiro-OMeTAD HTL and to find better *h*-ETL (hybrid electron transport layer) material that can improve the electron transport, the effect of different ETL (CdS, $Cd_{0.5}Zn_{0.5}S$, IGZO, and PCBM) and HTL

(CuSCN, MoO_3, CuO_2, and $MASnBr_3$) materials on the performance of the modeled solar cell was first investigated. The effect of ETL materials shows that the solar cell performs better when the ETL material has a wide bandgap, low activation energy, and an intense electric field at the ETL/Sb_2S_3 interface. The HTL material effect results show that HTL with both energy spike at Sb_2S_3/HTL interface and high hole mobility achieves better solar cell efficiency. Thus, cell efficiency and thermal stability were improved by selecting IGZO ETL and MoO_3 HTL materials to replace TiO_2 ETL and Spiro-OMeTAD HTL, respectively. Subsequently, the optimization of the new FTO/(ZnO/IGZO)/Sb_2S_3/MoO_3/Au solar cell shows that the greater thickness and bulk defect density in the Sb_2S_3 absorber and the greater defect density at the main junction interface increase the recombination rate in the solar cell. However, by reducing the number of recombination centers, higher acceptor concentrations compensate for these negative effects on cell performance. The HTL thickness has no effect on cell performance; conversely, thicker ETL material increases the width of the space charge region and the electric field at the ETL/absorber interface. In addition, it was found that higher shunt resistances overcome the negative effects of higher series resistances on performance parameters. For the higher efficiency, the optimum values obtained are 0.280 μm, 10^{10} cm^{-3}, and 10^{16} cm^{-3} for the thickness, bulk defect density, and doping of the Sb_2S_3 absorber, respectively; 0.03 μm for the thicknesses of the IGZO ETL; 10^6 cm^{-2} for the defect density of the h-ETL/Sb_2S_3 interface; and 4 $\Omega{\cdot}cm^2$ and 400 $\Omega{\cdot}cm^2$ for the series and shunt resistances, respectively. The combination of high performance and thermal stability of the device shows that three ranges of thermal stability exist for different metal work function. Finally, an efficiency of 15.43% and a temperature coefficient of -0.043%/K are obtained for the proposed FTO/(ZnO/IGZO)/Sb_2S_3/MoO_3/Ni device.

Data Availability

The data used to support the findings of this study are included within the article.

Conflicts of Interest

The authors declare that there is no conflict of interests regarding the publication of this paper.

Authors' Contributions

Pierre Gérard Darel Kond Ngue was responsible for the conceptualization, methodology, software, writing the original draft, validation, and project administration. Ariel Teyou Ngoupo was responsible for the conceptualization, methodology, software, writing the original draft, and validation. Aimé Magloire Ntouga Abena was responsible for the conceptualization, methodology, software, and writing the original draft. François Xavier Abomo Abega was responsible for the conceptualization, methodology, and software. Jean-Marie Bienvenu Ndjaka was responsible for the methodology, supervision, and validation. All authors read and approved the final manuscript.

Acknowledgments

The authors would like to extend their acknowledgement to the Gent University, Belgium, for developing and providing the SCAPS-1D simulator used in this work.

Supplementary Materials

Graphical representation of the energy band diagrams of the Sb_2S_3 solar cell associated with different ETL materials: (a) CdS ETL, (b) $Cd_{0.5}Zn_{0.5}S$ ETL, (c) IGZO ETL, and (d) PCBM ETL. Graphical representation of the generation profile, recombination profile, and electric field at the main junction of Sb_2S_3-based solar cell with different ETL materials. Sb_2S_3 solar cell electrical parameters (J_{SC}, V_{OC}, FF, and efficiency) tables for different ETL (CdS, $Cd_{0.5}Zn_{0.5}S$, IGZO, and PCBM)-HTL (MoO_3, $MASnBr_3$, Cu_2O, CuI, and CuSCN) material combinations. Graphical representation of normalized electrical parameters of FTO/(ZnO/TiO_2)/Sb_2S_3/Spiro-OMeTAD/Au and FTO/(ZnO/IGZO)/Sb_2S_3/MoO_3/Ni solar cells as function of operating temperature. Table of electrical parameters of Sb2S3 solar cell as a function of back metal contact. Table of thermal coefficient (CT) and efficiency (η) of a Sb_2S_3-based solar cell as a function of back contact type. *(Supplementary Materials)*

References

[1] M. F. Rahman, M. M. Moon, M. K. Hossain et al., "Concurrent investigation of antimony chalcogenide (Sb_2Se_3 and Sb_2S_3)-based solar cells with a potential WS_2 electron transport layer," *Heliyon*, vol. 8, no. 12, 2022.

[2] R. Kondrotas, C. Chen, and J. Tang, "Sb_2S_3 solar cells," *Joule*, vol. 2, no. 5, pp. 857–878, 2018.

[3] U. Chalapathi, B. Poornaprakash, C.-H. Ahn, and S.-H. Park, "Rapid growth of Sb_2S_3 thin films by chemical bath deposition with ethylenediamine tetraacetic acid additive," *Applied Surface Science*, vol. 451, pp. 272–279, 2018.

[4] C. Ma, H. Guo, X. Wang et al., "Fabrication of Sb_2Se_3 thin film solar cells by co-sputtering of Sb_2Se_3 and Se targets," *Solar Energy*, vol. 193, pp. 275–282, 2019.

[5] L. Zhang, K. Wu, J. Yu, Y. Yu, and Y. Wei, "Sb_2Se_3 films fabricated by thermal evaporation and post annealing," *Vacuum*, vol. 183, article 109840, 2021.

[6] F. Haidar, A. Pradel, Y. Chen, and M.-C. Record, "Deposition of Sb_2Se_3 thin films on Pt substrate via electro-chemical atomic layer epitaxy (EC-ALE)," *Journal of Electroanalytical Chemistry*, vol. 879, article 114774, 2020.

[7] L. Guo, B. Zhang, S. Li et al., "Scalable and efficient Sb_2S_3 thin-film solar cells fabricated by close space sublimation," *APL Materials*, vol. 7, no. 4, article 041105, 2019.

[8] C. Gao, J. Huang, H. Li et al., "Fabrication of Sb_2S_3 thin films by sputtering and post-annealing for solar cells," *Ceramics International*, vol. 45, no. 3, pp. 3044–3051, 2019.

[9] D.-H. Kim, S.-J. Lee, M. S. Park et al., "Highly reproducible planar Sb_2S_3-sensitized solar cells based on atomic layer deposition," *Nanoscale*, vol. 6, no. 23, pp. 14549–14554, 2014.

[10] J. Chenhui, R. Tang, X. Wang, H. Ju, G. Chen, and T. Chen, "Alkali metals doping for high-performance planar heterojunction Sb 2 S 3 solar cells," *Solar RRL*, vol. 3, article 1800272, 2018.

[11] J. Han, X. Pu, H. Zhou et al., "Synergistic effect through the introduction of inorganic zinc halides at the interface of TiO_2 and Sb_2S_3 for high-performance Sb_2S_3 planar thin-film solar cells," *ACS Applied Materials & Interfaces*, vol. 12, no. 39, pp. 44297–44306, 2020.

[12] A. Basak and U. P. Singh, "Numerical modelling and analysis of earth abundant Sb_2S_3 and Sb_2Se_3 based solar cells using SCAPS-1D," *Solar Energy Materials and Solar Cells*, vol. 230, article 111184, 2021.

[13] M. Courel, T. Jiménez, A. Arce-Plaza, D. Seuret-Jiménez, J. P. Morán-Lázaro, and F. J. Sánchez-Rodríguez, "A theoretical study on Sb_2S_3 solar cells: the path to overcome the efficiency barrier of 8%," *Solar Energy Materials and Solar Cells*, vol. 201, article 110123, 2019.

[14] M. T. Islam and A. K. Thakur, "Two stage modelling of solar photovoltaic cells based on Sb_2S_3 absorber with three distinct buffer combinations," *Solar Energy*, vol. 202, pp. 304–315, 2020.

[15] Y. Xiao, H. Wang, and H. Kuang, "Numerical simulation and performance optimization of Sb_2S_3 solar cell with a hole transport layer," *Optical Materials*, vol. 108, article 110414, 2020.

[16] M. S. Salem, A. Shaker, M. S. Othman, A. H. Al-Bagawia, M. Fedawy, and G. M. Aleid, "Numerical analysis and design of high performance HTL-free antimony sulfide solar cells by SCAPS-1D," *Optical Materials*, vol. 123, article 111880, 2022.

[17] S. Barthwal, R. Gupta, A. Kumar, K. Ramesh, S. Pathak, and S. Karak, "Band offset engineering in antimony sulfide (Sb_2S_3) solar cells, using SCAPS simulation: a route toward PCE >10%," *Optik*, vol. 282, article 170868, 2023.

[18] J. Chen, J. Zhang, C. Huang, Z. Bi, X. Xu, and H. Yu, "SnO2/2D-Bi2O2Se new hybrid electron transporting layer for efficient and stable perovskite solar cells," *Chemical Engineering Journal*, vol. 410, article 128436, 2021.

[19] P. Subudhi and D. Punetha, "Pivotal avenue for hybrid electron transport layer-based perovskite solar cells with improved efficiency," *Scientific Reports*, vol. 13, 2023.

[20] F. Wang, Y. Zhang, J. Du et al., "Exploring low-temperature processed a-WOx/SnO2 hybrid electron transporting layer for perovskite solar cells with efficiency >20.5%," *NaEnergy*, vol. 63, article 103825, 2019.

[21] W. Chai, W. Zhu, D. Chen et al., "Combustion-processed NiO/ALD TiO2 bilayer as a novel low-temperature electron transporting material for efficient all-inorganic CsPbIBr2 solar cell," *Solar Energy*, vol. 203, pp. 10–18, 2020.

[22] X. Xu, H. Zhang, J. Shi et al., "Highly efficient planar perovskite solar cells with a TiO_2/Zelectron transport bilayer," *Journal of Materials Chemistry A*, vol. 3, no. 38, pp. 19288–19293, 2015.

[23] A. Baron Jaimes, O. A. Jaramillo-Quintero, R. A. Miranda Gamboa, A. Medina-Flores, and M. E. Rincon, "Functional ZnO/TiO_2 bilayer as electron transport material for solution-processed Sb_2S_3 solar cells," *Solar RRL*, vol. 5, no. 3, p. 2000764, 2021.

[24] S. Ijaz, E. Raza, Z. Ahmad et al., "Numerical simulation to optimize the efficiency of HTM-free perovskite solar cells by ETM engineering," *Solar Energy*, vol. 250, pp. 108–118, 2023.

[25] M. K. Hossain, G. F. Toki, I. Alam et al., "Numerical simulation and optimization of $CsPbI_3$-based perovskite solar cell to enhance the power conversion efficiency," *New Journal of Chemistry*, vol. 47, pp. 4801–4817, 2023.

[26] M. Islam, M. R. Islam, S. Ahmmed, M. K. Hossain, and M. Rahman, "Highly efficient SnS-based inverted planar heterojunction solar cell with ZETL," *Physica Scripta*, vol. 98, no. 6, article 065501, 2023.

[27] A.-A. Kanoun, M. B. Kanoun, A. E. Merad, and S. Goumri-Said, "Toward development of high-performance perovskite solar cells based on CH3NH3GeI3 using computational approach," *Solar Energy*, vol. 182, pp. 237–244, 2019.

[28] K. K. Maurya and V. N. Singh, "Sb_2Se_3/CZTS dual absorber layer based solar cell with 36.32 % efficiency: a numerical simulation," *Journal of Science: Advanced Materials and Devices*, vol. 7, no. 2, article 100445, 2022.

[29] A. Tara, V. Bharti, S. Sharma, and R. Gupta, "Computational approach to explore suitable charge transport layers for all inorganic $CsGeI_3$ perovskite solar cells," *Optical Materials*, vol. 128, article 112403, 2022.

[30] Y. Z. Hamri, Y. Bourezig, M. Meldes et al., "Improved efficiency of Cu(In, Ga)Se_2 thinfilm solar cells using a buffer layer alternative to CdS," *Solar Energy*, vol. 178, pp. 150–156, 2019.

[31] A. Hima, N. Lakhdar, B. Benhaoua, A. Saadoune, I. Kemerchou, and F. Rogti, "An optimized perovskite solar cell designs for high conversion efficiency," *Superlattices and Microstructures*, vol. 129, pp. 240–246, 2019.

[32] S. Zandi, P. Saxena, and N. E. Gorji, "Numerical simulation of heat distribution in RGO-contacted perovskite solar cells using COMSOL," *Solar Energy*, vol. 197, pp. 105–110, 2020.

[33] A. Bag, R. Radhakrishnan, R. Nekovei, and R. Jeyakumar, "Effect of absorber layer, hole transport layer thicknesses, and its doping density on the performance of perovskite solar cells by device simulation," *Solar Energy*, vol. 196, pp. 177–182, 2020.

[34] B. S. Roshi and V. Gupta, "Modelling and simulation of silicon solar cells using PC1D," *Materials Today: Proceedings*, vol. 54, pp. 810–813, 2022.

[35] I. Gharibshahian, A. A. Orouji, and S. Sharbati, "Towards high efficiency Cd-Free Sb_2Se_3 solar cells by the band alignment optimization," *Solar Energy Materials and Solar Cells*, vol. 212, article 110581, 2020.

[36] M. Burgelman, P. Nollet, and S. Degrave, "Modelling polycrystalline semiconductor solar cells," *Thin Solid Films*, vol. 361-362, pp. 527–532, 2000.

[37] A. M. N. Abena, A. T. Ngoupo, F. X. A. Abega, and J. M. B. Ndjaka, "Numerical investigation of solar cells based on hybrid organic cation perovskite with inorganic HTL via SCAPS-1D," *Chinese Journal of Physics*, vol. 76, pp. 94–109, 2022.

[38] J. Madan, S. Gohri, R. Pandey, and R. Sharma, "Device simulation of 17.3% efficient lead-free all-perovskite tandem solar cell," *Solar Energy*, vol. 197, pp. 212–221, 2020.

[39] A. T. Ngoupo, S. Ouédraogo, F. Zougmoré, and J. M. B. Ndjaka, "Numerical analysis of ultrathin Sb_2Se_3-based solar cells by SCAPS-1D numerical simulator device," *Chinese Journal of Physics*, vol. 70, pp. 1–13, 2021.

[40] V. Odari, R. Musembi, and J. Mwabora, "Device simulation of Sb_2S_3 solar cells by SCAPS-1D software, févr. 2019. Consulté le: 9 avril 2023," Disponible sur: http://www.semanticscholar.org/paper/Device-Simulation-of-Sb2S3-Solar-Cells-by-SCAPS-1D-Odari-Musembi/5275c2841bbb3bc96aab47c5190c1104e3213550.

[41] N. Singh, A. Agarwal, and M. Agarwal, "Numerical simulation of highly efficient lead-free all-perovskite tandem solar cell," *Solar Energy*, vol. 208, pp. 399–410, 2020.

[42] N. K. Singh, A. Agarwal, A. K. Singh, and S. N. Singh, "Design and performance evaluation of eco-friendly $FASnI_3$/$CsSn_{0.5}Ge_{0.5}I_3$ based perovskite solar cell with distinct charge transport layer: A computational modeling," *Solar Energy*, vol. 268, article 112256, 2024.

[43] S. Abdelaziz, A. Zekry, A. Shaker, and M. Abouelatta, "Investigation of lead-free $MASnI_3$-$MASnIBr_2$ tandem solar cell: numerical simulation," *Optical Materials*, vol. 123, article 111893, 2022.

[44] F. Ayala-Mato, O. Vigil-Galán, M. Courel, and M. M. Nicolás-Marín, "Analysis of the efficiency in Sb_2Se_3 thin-film solar cells using alternative buffer layers in n-p and n-i-p structures by numerical simulation," in *In Review*, preprint, 2021.

[45] M. S. S. Basyoni, M. M. Salah, M. Mousa et al., "On the investigation of interface defects of solar cells: lead-based vs lead-free perovskite," *IEEE Access*, vol. 9, pp. 130221–130232, 2021.

[46] S. Bouazizi, W. Tlili, A. Bouich, B. M. Soucase, and A. Omri, "Design and efficiency enhancement of FTO/PC $_{60}$ BM/CsSn $_{0.5}$ Ge $_{0.5}$ I $_3$/Spiro-OMeTAD/Au perovskite solar cell utilizing SCAPS-1D simulator," *Materials Research Express*, vol. 9(9), article 096402, 2022.

[47] C. Chen and J. Tang, "Open-circuit voltage loss of antimony chalcogenide solar cells: status, origin, and possible solutions," *ACS Energy Letters*, vol. 5, no. 7, pp. 2294–2304, 2020.

[48] Y. Gan, X. Bi, Y. Liu et al., "Numerical investigation energy conversion performance of tin-based perovskite solar cells using cell capacitance simulator," *Energies*, vol. 13, no. 22, p. 5907, 2020.

[49] A. Kumar and S. Singh, "Numerical modeling of lead-free perovskite solar cell using inorganic charge transport materials," *Materials Today: Proceedings*, vol. 26, pp. 2574–2581, 2020.

[50] D. Stanić, V. Kojić, T. Cizmar et al., "Simulating the performance of a formamidinium based mixed cation lead halide perovskite solar cell," *Materials*, vol. 14, no. 21, p. 6341, 2021.

[51] M. K. Hossain, D. P. Samajdar, R. C. Das et al., "Design and simulation of Cs2BiAgI6 double perovskite solar cells with different electron transport layers for efficiency enhancement," *Energy Fuels*, vol. 37, no. 5, pp. 3957–3979, 2023.

[52] J. Prakash, A. Singh, G. Sathiyan et al., "Progress in tailoring perovskite based solar cells through compositional engineering: materials properties, photovoltaic performance and critical issues," *Materials Today Energy*, vol. 9, pp. 440–486, 2018.

[53] T. Minemoto and M. Murata, "Theoretical analysis on effect of band offsets in perovskite solar cells," *Solar Energy Materials and Solar Cells*, vol. 133, pp. 8–14, 2015.

[54] D. Dastan, M. Mohammed, A. K. Al-Mousoi et al., "Insights into the photovoltaic properties of indium sulfide as an electron transport material in perovskite solar cells," *Scientific Reports*, vol. 13, p. 1, 2023.

[55] M. K. Hossain, A. A. Arnab, D. P. Samajdar et al., "Design insights into La_2NiMnO_6-based perovskite solar cells employing different charge transport layers: DFT and SCAPS-1D frameworks," *Energy Fuels*, vol. 37, no. 17, pp. 13377–13396, 2023.

[56] M. K. Hossain, G. F. I. Toki, A. Kuddus et al., "An extensive study on multiple ETL and HTL layers to design and simulation of high-performance lead-free $CsSnCl_3$-based perovskite solar cells," *Scientific Reports*, vol. 13, no. 1, 2023.

[57] M. K. Hossain, M. Mohammed, R. Pandey et al., "Numerical analysis in DFT and SCAPS-1D on the influence of different charge transport layers of $CsPbBr_3$ perovskite solar cells," *Energy Fuels*, vol. 37, no. 8, pp. 6078–6098, 2023.

[58] M. K. Hossain, G. F. I. Toki, D. P. Samajdar et al., "Deep insights into the coupled optoelectronic and photovoltaic analysis of lead-free $CsSnI_3$ perovskite-based solar cell using DFT calculations and SCAPS-1D simulations," *ACS Omega*, vol. 8, no. 25, pp. 22466–22485, 2023.

[59] L. Et-taya, T. Ouslimane, and A. Benami, "Numerical analysis of earth-abundant $Cu_2ZnSn(S_xSe_{1-x})_4$ solar cells based on spectroscopic ellipsometry results by using SCAPS-1D," *Solar Energy*, vol. 201, pp. 827–835, 2020.

[60] H. Luo, Y. Zhang, and H. Li, "Effect of MoS_2 interlayer on performances of copper-barium-tin-sulfur thin film solar cells via theoretical simulation," *Solar Energy*, vol. 223, pp. 384–397, 2021.

[61] M. Djinkwi Wanda, S. Ouédraogo, F. Tchoffo, F. Zougmoré, and J. M. B. Ndjaka, "Numerical investigations and analysis of Cu_2ZnSnS_4 based solar cells by SCAPS-1D," *International Journal of Photoenergy*, vol. 2016, Article ID 2152018, 9 pages, 2016.

[62] T. Ouslimane, L. Et-taya, L. Elmaimouni, and A. Benami, "Impact of absorber layer thickness, defect density, and operating temperature on the performance of $MAPbI_3$ solar cells based on Zelectron transporting material," *Heliyon*, vol. 7, no. 3, article e06379, 2021.

[63] N. Gamal, S. H. Sedky, A. Shaker, and M. Fedawy, "Design of lead-free perovskite solar cell using $Zn_{1-x}Mg_xO$ as ETL: SCAPS device simulation," *Optik*, vol. 242, article 167306, 2021.

[64] T. K. Tulka, N. Alam, M. Akhtaruzzaman, K. Sobayel, and M. M. Hossain, "Optimization of a high-performance lead-free cesium-based inorganic perovskite solar cell through numerical approach," *Heliyon*, vol. 8, no. 11, article e11719, 2022.

[65] S. R. A. Ahmed, A. Sunny, and S. Rahman, "Performance enhancement of Sb_2Se_3 solar cell using a back surface field layer: a numerical simulation approach," *Solar Energy Materials and Solar Cells*, vol. 221, article 110919, 2021.

[66] P. Singh and N. M. Ravindra, "Temperature dependence of solar cell performance—an analysis," *Solar Energy Materials and Solar Cells*, vol. 101, pp. 36–45, 2012.

[67] R. A. Street, M. Schoendorf, A. Roy, and J. H. Lee, "Interface state recombination in organic solar cells," *Physical Review B*, vol. 81, no. 20, article 205307, 2010.

[68] S. Chander, A. Purohit, A. Sharma, S. P. Nehra, and M. S. Dhaka, "A study on photovoltaic parameters of monocrystalline silicon solar cell with cell temperature," *Energy Reports*, vol. 1, pp. 104–109, 2015.

[69] N. K. Singh, A. Agarwal, T. Kanumuri, and T. Varshney, "A study of an inorganic-organic HTM on the implementation of lead based PSC device," in *2020 IEEE Students Conference on Engineering & Systems (SCES)*, Prayagraj, India, 2020.

[70] F. F. Muhammad and K. Sulaiman, "Photovoltaic performance of organic solar cells based on DH6T/PCBM thin film active layers," *Thin Solid Films*, vol. 519, no. 15, pp. 5230–5233, 2011.

[71] F. F. Muhammad, M. Y. Yahya, S. S. Hameed et al., "Employment of single-diode model to elucidate the variations in photovoltaic parameters under different electrical and thermal conditions," *PLoS ONE*, vol. 12, no. 8, article e0182925, 2017.

[72] G. N. Derry, M. E. Kern, and E. H. Worth, "Recommended values of clean metal surface work functions," *Journal of*

Vacuum Science & Technology A: Vacuum, Surfaces, and Films, vol. 33, no. 6, article 060801, 2015.

[73] N. Rai, S. Rai, P. K. Singh, P. Lohia, and D. K. Dwivedi, "Analysis of various ETL materials for an efficient perovskite solar cell by numerical simulation," *Journal of Materials Science: Materials in Electronics*, vol. 31, no. 19, pp. 16269–16280, 2020.

[74] F. A. Jhuma, M. Z. Shaily, and M. J. Rashid, "Towards high-efficiency CZTS solar cell through buffer layer optimization," *Materials for Renewable and Sustainable Energy*, vol. 8, no. 1, p. 6, 2019.

[75] H. Chen, Z.-Q. Li, B. Sun, and X.-D. Feng, "Towards high-efficiency planar heterojunction antimony sulfide solar cells," *Optical Materials*, vol. 121, article 111556, 2021.

[76] S. Yuan, H. Deng, D. Dong et al., "Efficient planar antimony sulfide thin film photovoltaics with large grain and preferential growth," *Solar Energy Materials and Solar Cells*, vol. 157, pp. 887–893, 2016.

[77] X. Chen, Z. Li, H. Zhu et al., "CdS/Sb_2S_3 heterojunction thin film solar cells with a thermally evaporated absorber," *Journal of Materials Chemistry C*, vol. 5, no. 36, pp. 9421–9428, 2017.

[78] K. Wang, J. Cheng, X. Yang et al., "Enhanced Photovoltaic Properties in Sb_2S_3 planar heterojunction solar cell with a fast selenylation approach," *Nanoscale Research Letters*, vol. 13, no. 1, p. 270, 2018.

[79] G. Pan, D. Wang, S. Gao et al., "Substrate structured Sb_2S_3 thin film solar cells fabricated by rapid thermal evaporation method," *Solar Energy*, vol. 182, pp. 64–71, 2019.